

Dynamical Learning in Deep Asymmetric Recurrent Neural Networks

Davide Badalotti, Carlo Baldassi, Marc Mézard, Mattia Scardecchia, and Riccardo Zecchina
Department of Computing Sciences, Bocconi University, Milan, Italy

We show that asymmetric deep recurrent neural networks, enhanced with additional sparse excitatory couplings, give rise to an exponentially large, dense accessible manifold of internal representations which can be found by different algorithms, including simple iterative dynamics. Building on the geometrical properties of the stable configurations, we propose a distributed learning scheme in which input-output associations emerge naturally from the recurrent dynamics, without any need of gradient evaluation. A critical feature enabling the learning process is the stability of the configurations reached at convergence, even after removal of the supervisory output signal. Extensive simulations demonstrate that this approach performs competitively on standard AI benchmarks. The model can be generalized in multiple directions, both computational and biological, potentially contributing to narrowing the gap between AI and computational neuroscience.

The impressive performance of artificial intelligence (AI) systems, driven by large-scale artificial neural networks, have stimulated intense research efforts aimed at understanding their underlying computational principles. Modern AI architectures, such as deep convolutional networks [1], diffusion-based generative models [2], and autoregressive transformers [3] used in language models, are trained on huge datasets and rely on gradient-based optimization, which is energy intensive. Moreover, they do not attempt to exploit the rich dynamical behavior offered by more realistic recurrent networks. Many in the field of computational neuroscience view current AI approaches as not well aligned with the goal of explaining computation in neural circuits [4, 5]. Understanding how biological systems perform complex learning tasks efficiently without explicitly computing high-dimensional gradients is thus a central question. In recent years, this problem has been addressed by replacing global error signals and backpropagation with local learning rules (e.g., random feedback [6] or target-based signals [7, 8]) or dynamics-based updates (e.g., predictive coding [9], equilibrium propagation [10], or reservoir computing [11]) and spiking neural networks [12]. These approaches differ in scope, but they all emphasize aspects such as locality, efficiency, and biological plausibility.

In this work we introduce a novel model that implements a simple, fully distributed learning mechanism grounded in the dynamics of asymmetric deep recurrent networks. It exploits the existence of an accessible, dense connected cluster of stable fixed points – a high local entropy region [13] – which is key for implementing distributed, gradient-free learning schemes. For readability, we will refer to this structure as the internal Representation Manifold (RM).

Our model is based on a core module which is a network of binary neurons interacting with asymmetric couplings. While these models have been studied for long in the context of computational neuroscience, most of the studies have focused on their chaotic regime [14], or on the edge of chaos, for signal processing applications. Here we introduce an excitatory self-coupling in the core

module, or alternatively some sparse and strong excitatory couplings between several core modules. This simple modification, with well-tuned strength of the excitation, leads to the appearance of a RM which provide an exponentially large number of accessible internal representations. We show that this structure can be exploited via a learning protocol for supervised learning that does not require gradient information. Instead, learning is solely based on the local information available to neurons and does not require any additional feedback circuit. Input-output associations are formed through the recurrent network dynamics. The working principle of the model differs from that of Hopfield-like networks [15], which rely on the existence of fixed points induced by symmetric couplings. It also differs from the asymmetric networks studied so far in computational neuroscience [14, 16].

The paper is organized as follows: First, we define the model and the statistical mechanics analysis concerning the onset of the RM, based on the local entropy method [13]. Next, we define the learning processes and present the results of extensive numerical experiments. Finally, we conclude with a numerical check on the role of the RM and the role of symmetry.

Core Module. The core module is a network of binary neurons with state $s \in \{-1, 1\}^N$ and a $N \times N$ asymmetric interaction matrix J . The off-diagonal matrix elements $J_{ij}, i \neq j$ are drawn independently from an unbiased Gaussian distribution of variance $\frac{1}{N}$. We introduce a self-interaction term $J_{ii} = J_D \geq 0$ for all i , which softens the fixed-point constraints and controls the dynamics. The network evolves in discrete time by aligning each neuron to its local field through the update rule:

$$s_i \leftarrow \text{sgn}\left(\sum_{j \neq i} J_{ij} s_j + J_D s_i\right), \quad (1)$$

with sgn being the sign function. Throughout this study, unless otherwise specified, we will adopt a synchronous dynamical scheme for the updates. Due to the asymmetry of the interactions, the dynamics is not governed by a Lyapunov function. The simplicity of the dynamical rule and the lack of forced symmetry in the synapses

make this module potentially appealing also from a biological perspective. As we shall see, while for $J_D = 0$ the network is chaotic and no fixed-points exist, for $J_D > 0$ there exist exponentially many fixed points. However they remain unreachable to the dynamics until the RM appears, for J_D large enough. This behavior is reminiscent to what was found in other settings [13, 17–19], in the context of learning in non convex classifiers.

Multilayer Chain As a minimal model of hierarchical processing, we consider a chain of L core modules like the one above, with states $s^{(l)} \in \{-1, 1\}^N$, and independent interaction matrices $J^{(l)} \in \mathbb{R}^{N \times N}$, $l = 1, \dots, L$. We introduce a positive interaction between homologous neurons in adjacent layers with uniform strength $\lambda \geq 0$:

$$s_i^{(l)} \leftarrow \text{sgn} \left(\sum_{j \neq i} J_{ij}^{(l)} s_j^{(l)} + J_D s_i^{(l)} + \lambda (s_i^{(l-1)} + s_i^{(l+1)}) \right), \quad (2)$$

with the understanding that $s_i^{(0)} \equiv s_i^{(L+1)} \equiv 0$. This reduces to the core model for $L = 1$. As we shall see, the excitatory sparse interactions across modules governed by λ play a role very similar to the diagonal coupling J_D . 1 provides a sketch of the chain.

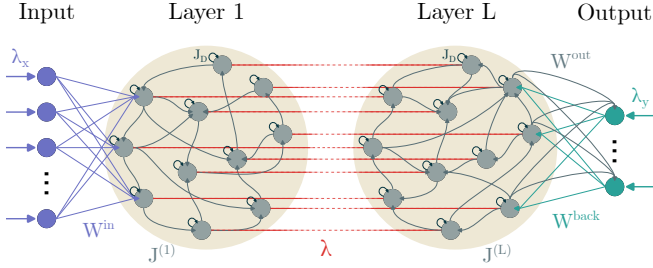


FIG. 1: A multilayer chain model with sparse inter module excitatory couplings, and input/output layers.

Local learning process: Learning is implemented by adding trainable input and output layers, which serve as the interface between external data and the internal network dynamics (see Fig. 1). These layers influence the overall dynamics of the system and are trained jointly with the internal networks using local learning rules. It is worth noting that these learning models can be extended to more complex architectures. Preliminary tests indicate that, provided a RM is present, the system exhibits nontrivial learning capabilities based on local adaptation mechanisms.

Analysis of the geometry of fixed points: To analyze the geometric structure of the fixed points and their accessibility, we begin by computing the typical number \mathcal{N}_{fp} of fixed points. This number being exponentially large, we shall compute the associated entropy density $S_{\text{fp}} = \lim_{N \rightarrow \infty} \frac{1}{2N} \log \mathcal{N}_{\text{fp}}$. As S_{fp} is expected to self-average, we are interested in the quenched average $\frac{1}{N} \mathbb{E} \log \mathcal{N}_{\text{fp}}$, where \mathbb{E} denotes the expectation value with respect to the distribution of off-diagonal couplings J_{ij} .

It turns out that in the large N limit the ‘annealed average’, i.e. the easily-computed first-moment upper bound $\frac{1}{N} \log \mathbb{E} \mathcal{N}_{\text{fp}}$ is tight for the core model and for $L = 2$. For instance, for the two layer case we find:

$$S_{\text{fp}} = \lim_{N \rightarrow \infty} \frac{1}{2N} \log \overline{\mathcal{N}}_{\text{fp}} = \frac{\log 2}{2} + \frac{1}{2} \log \left[H(-J_D - \lambda)^2 + H(-J_D + \lambda)^2 \right] \quad (3)$$

where $H(x) = \frac{1}{2} \text{Erfc} \left(\frac{x}{\sqrt{2}} \right)$. The entropy S_{fp} is an increasing function of J_D and λ , it vanishes when $J_D = \lambda = 0$, and goes to $\log 2$ in the limit $J_D, \lambda \rightarrow \infty$, where all configurations become fixed points. The core model is recovered by setting $\lambda = 0$. Details of the derivation are given in the Supplementary Material (SM). A replica computation of the same quantity confirms that the fixed points are isolated and point-like (see SM). According to the overlap gap property (OGP) [20], this implies that stable algorithms (which include the network dynamics as a specific case) cannot reach such fixed-point configurations in sub-exponential time, assuming these are the only solutions present. As discussed in ref. [13], while these analytical calculations correctly give the behavior of dominant configurations, they neglect the role of subdominant configurations which are not isolated and can be attractive for some dynamical processes and algorithms. Extensive simulations with several algorithms [21] show that there exist algorithm-dependent threshold values of J_D beyond which fixed points can be reached very rapidly. For the core model, Belief Propagation with reinforcement [17] appears to be able to find fixed points with J_D as low as 0.35 for large N in a small (sublinear) number of iterations; likelihood optimization à la ref. [22] seems to require $J_D \gtrsim 0.5$; simple iteration of the update dynamics $J_D \gtrsim 0.8$. This regime is characterized by an extended connected cluster with a high density of solutions and a branching structure [18, 23], which can be studied by a more refined analytical approach where one biases the Gibbs measure toward fixed points surrounded by a large number of neighboring solutions [13]. This “Local Entropy approach” uses an effective energy density $\mathcal{E}(\tilde{s}, d)$ relative to a reference configuration of the neurons \tilde{s} , and the associated partition function defined as

$$\mathcal{E}(\tilde{s}, d) = -\frac{1}{N} \log \mathcal{N}(\tilde{s}, d) ; \quad Z(d, y) = \sum_{\tilde{s}} e^{-y N \mathcal{E}(\tilde{s}, d)} \quad (4)$$

where $\mathcal{N}(\tilde{s}, d)$ is the number of solutions s at normalized Hamming distance d from \tilde{s} , and the parameter y plays the role of an inverse temperature, controlling the reweighting of the local entropy contribution. The corresponding free energy density

$$\Phi(d, y) = -\lim_{N \rightarrow \infty} \frac{1}{Ny} \log Z(d, y) \quad (5)$$

allows to reveal sub-dominant regions with highest density of fixed points in the limit of large y and small d . Relevant quantities are the average local entropy, i.e. the internal entropy density of the RM, $S_I(d, y) \equiv \langle \mathcal{E} \rangle = -\frac{\partial}{\partial y} [y\Phi(d, y)]$ and the log of number of such regions, called the “external entropy density”, $S_E(d, y) = -y(\Phi(d, y) + S_I(d, y))$. At fixed d , S_I is an increasing function of y and S_E is a decreasing function.

As explained in ref. [13], the signature of the existence of an accessible RM is that, at the largest value of y for which the external entropy $S_E(d, y) \geq 0$, the internal entropy $S_I(d, y) > 0$ in a neighborhood of $d = 0$. The case $y = 1$ reduces to the computation of the entropy surrounding typical fixed points, which in our case would be the isolated ones. Considering values of $y > 1$ implies that we are exploring subdominant regions or out-of-equilibrium states.

We evaluate Eq. 5 in the large N limit, using the replica method under the replica symmetric (RS) Ansatz. As discussed in ref. [24], this computation can be formally interpreted as the one-step replica symmetry breaking (1-RSB) calculation of the original problem of computing the entropy of fixed points, where now the Parisi parameter m must be identified with y , and the internal overlap q_1 is used as a control parameter to fix the region’s diameter via $d = (1 - q_1)/2$.

The asymptotic expression for the free energy and related entropies can be derived for an arbitrary number of layers, see SM. However solving the saddle point equations poses difficult numerical challenges, and we limit our analytical study to the case of two layers, which is enough to display the role of both J_D and λ . The expression for the free energy density reads:

$$-y\Phi(d, y) = -\hat{q}_1 + (1 - y)\hat{q}_1 q_1 + \frac{1}{y} \log \left\{ \int Dz Dz' Dt Dt' \left[\sum_{s, s' \in \{\pm 1\}} e^{\sqrt{\hat{q}_1}(st + s't')} H \left(\frac{-J_D + \lambda ss' - s\sqrt{\hat{q}_1}z}{\sqrt{1 - q_1}} \right) \times H \left(\frac{-J_D + \lambda ss' - s'\sqrt{\hat{q}_1}z'}{\sqrt{1 - q_1}} \right) \right]^y \right\} \quad (6)$$

where Dz, Dz', Dt, Dt' are Gaussian measures with mean 0 and variance 1, and \hat{q}_1 is determined by the saddle point equation $\partial\Phi/\partial\hat{q}_1 = 0$ (see SM). The results for the core and multilayer chain models are as follows.

Consider the single core module. The free energy density is recovered by setting $\lambda = 0$ and dividing by 2 (to account for the number of neurons). Solving the saddle-point equations reveals that, for all $J_D > 0$ and d , there exists a value of y beyond which the external entropy $S_E(d, y)$ becomes negative. This is unphysical and indicates a breakdown of the RS assumption, signaling a discontinuous phase transition. To identify the critical values of J_D , we first compute, for each value of d ,

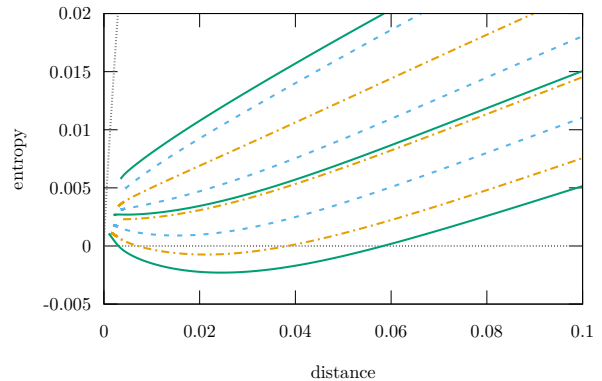


FIG. 2: Internal entropy (divided by L) for the Core Model (solid green) and two-layer model (dashed/dot-dashed blue/orange). Core Model: $J_D = 0.05, 0.07, 0.1$ (bottom to top). Two-layer: blue ($J_D = 0.05$) with $\lambda = 0.2, 0.3, 0.4$ (bottom to top); orange ($J_D = 0$) with $\lambda = 0.4, 0.45, 0.5$ (bottom to top). All curves vanish at distance 0 (not shown due to numerical limits). In all cases, increasing J_D or λ drives the OGP–RM transition.

the value y^* at which the external entropy vanishes, and next seek the value of J_D below which the internal entropy becomes a non-monotonic function of the distance. We find that the phase space separates in two regions. For all $J_D < J_{Dc} \simeq 0.07$, the internal entropy is non-monotonic. The value of $d = (1 - q_1)/2$ that maximizes the entropy coincides with the self-overlap of subdominant states, given that the associated value of y^* exceeds one. The actual values of d are extremely small (see SM), suggesting that finding fixed points belonging to such states would still be hard for local algorithms. For all $J_D > J_{Dc}$, the internal entropy increases monotonically with d , eventually saturating at a plateau equal to the entropy of typical solutions. This behavior indicates the existence of an extensive cluster in configuration space where fixed points coalesce giving rise to the RM geometry.

The same analysis can be extended to the multilayer model. Focusing on the case of $L = 2$, we find that the role of λ closely parallels that of J_D : a positive sparse coupling λ between different subsystems induces the emergence of a RM. Specifically, for small values of J_D , including zero, a critical value of $\lambda \lesssim 0.45$ exists at which the extended high-density cluster of fixed points emerges. Fig. 2 shows the behavior of the local entropy for the two cases.

The existence of the RM is a necessary condition for the convergence of local algorithms. A more refined analysis can be performed along the lines of ref. [19]. While we have checked convergence for different local algorithms (SM and [21]), here we shall focus solely on the simple update dynamics and exploit its convergence and

stability features for learning.

Learning: For simplicity, we shall describe a supervised learning protocol on the Core Module; the generalization to multilayer architectures is straightforward and can be found in the Supplementary Material (SM). The algorithm aims to map input-output pairs onto internal representations by steering the spontaneous neural dynamics through external fields and stabilizing it through a local plasticity rule. Assume that we are provided with a set of P patterns with their associated labels $\{x^\mu, y^\mu\}_{\mu=1}^P$ with $x^\mu \in \mathbb{R}^D, y^\mu \in \mathbb{R}^C$. We consider two projection matrices $W^{\text{in}} \in \mathbb{R}^{N \times D}, W^{\text{back}} \in \mathbb{R}^{N \times C}$ that mediate the influence of the input and label onto the network state (see Fig. 1), as well as a readout matrix $W^{\text{out}} \in \mathbb{R}^{C \times N}$ that outputs a prediction given the state of the network. In general, it is not necessary that all neurons be affected by the input or supervisory signal, nor that they all affect the predicted output. We encode this with binary vectors $a^{\text{in}}, a^{\text{back}}, a^{\text{out}} \in \{0, 1\}^N$.

During training, pairs x^μ, y^μ are presented one at a time. The network evolves in parallel by aligning neurons to their local field, under the influence of the input and with supervision from the label:

$$s_i \leftarrow \text{sgn} \left(\sum_{j=1}^N J_{ij} s_j + a_i^{\text{in}} \lambda_x \sum_{k=1}^D W_{ik}^{\text{in}} x_k^\mu + a_i^{\text{back}} \lambda_y \sum_{c=1}^C W_{ic}^{\text{back}} y_c^\mu \right). \quad (7)$$

Neurons are initialized by the input and output external signals in the first dynamical step. This is equivalent to initializing $s_i := 0 \ \forall i$ in the parallel update dynamics. Once the system reaches an equilibrium, the supervisory signal is removed (by setting $\lambda_y = 0$), and the dynamics continues until a new fixed point is reached. This two-phase process can be interpreted as a simplified model of the onset and subsequent fading of a transient external stimulus to the network. Such a stimulus could correspond to a sensory input, or alternatively to the activity of another, unmodeled supervisory network. Let s^* denote the internal state reached at the end of the second phase. To stabilize s^* , we apply a local plasticity rule inspired by the perceptron learning rule. Specifically, the rule increases the stability margin of each neuron by $\eta > 0$ whenever it falls below a threshold $\kappa > 0$:

$$h_i = \sum_{j=1}^N J_{ij} s_j^* + a_i^{\text{in}} \lambda_x \sum_{k=1}^D W_{ik}^{\text{in}} x_k^\mu \quad (8)$$

$$J_{ij} \leftarrow J_{ij} + \eta s_i^* s_j^* \mathbb{1}(s_i^* \cdot h_i \leq \kappa) \quad (9)$$

The projection W^{in} can be learned using the exact same rule, with x_k^μ playing the role of s_k^* . The readout matrix W^{out} can be trained to predict y^μ from s^* using any appropriate method. Here we employ the perceptron learning rule also for W^{out} . During inference, we let

the network relax under the influence of the input only, and upon convergence to a state \hat{s} we use the learned W^{out} to compute a prediction \hat{y} from the final network state.

Note that the dynamics can be truncated after a fixed number of steps, instead of waiting until convergence, and the learning rule will tend to make the final state a fixed point. In practice, after the first few learning steps, the dynamics usually converges in a very small number of sweeps. Furthermore, learning can be made faster using batches of examples (see SM).

Performance Benchmarks. To validate our proposed approach, we conducted experiments on a compressed version of the MNIST dataset, that we refer to as Entangled-MNIST. The dataset is obtained by flattening the original MNIST images into vectors of dimension 784. Each vector is then projected onto a 100-dimensional subspace using a (fixed) random linear projection and later binarized to ± 1 element-wise. The final dataset consists of $P = 60000$ training instances and $P_{\text{eval}} = 10000$ validation instances of size $D = 100$, equally divided between $C = 10$ classes. This process creates a more challenging learning scenario compared to the original MNIST, that tests the robustness of models operating on compressed and structurally entangled data, on which linear classifiers have poor performance (see SM).

We train our models with $L = 1$ and N between 100 and 6400 for a total of 200 epochs (details are given in the SM). Performance is evaluated in terms of average training and validation accuracy, with comparisons made against two baseline methods that restrict learning to the readout layer on top of frozen features. The first baseline is a reservoir computing model [25], - which runs the network dynamics but excludes plasticity in the J matrix. Although it leverages internal representations of the initial random couplings J_{ij} , it lacks the ability to adapt them to the task. The second baseline is a random features model, which reduces the dynamics to a single update step, effectively implementing a random nonlinear projection from D to N dimensions. The results of these comparisons are presented in Figure 3. Our model outperforms both baselines in training and validation accuracy, highlighting the effectiveness of the proposed training procedure even for challenging datasets with entangled structure. Since the number of adjustable parameters scales quadratically with N , we do not regard these numerical comparisons as a measure of absolute performance with respect to models that have a number of parameters that scales linearly in N . Our goal here is restricted to demonstrating the efficacy of the learning procedure. A benchmarking analysis against state-of-the-art models will be presented in [21].

On the role of the RM To shed some light on the importance of the RM accessibility unveiled by the theoretical analysis, we carried out two sets of experiments, detailed in the SM. In the first experiment, we measured

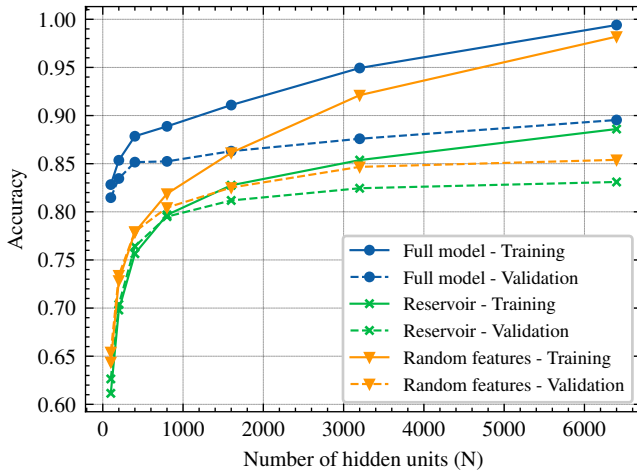


FIG. 3: Accuracy on Entangled-MNIST vs. core size N . Our model (blue), reservoir computing (green) and random features classifiers (orange).

how the performance of our algorithm depends on the couplings J_D and λ , in the case $L = 2$. The network is unable to learn the task when J_D and λ are too small, but its performance drastically improves as J_D or λ increase, coherently with the onset of the RM (at least at network initialization). If J_D or/and λ become too large, the recurrent modules implement the identity function and the performance drops. In the second experiment, we compare the performance of the asymmetric single-layer model of the previous section with that of symmetric variants, using a symmetric initialization for the coupling matrix and variants of the plasticity rule that preserve the symmetry. With $J_D = 0$, the dynamics descends a Lyapunov function and is convergent. Remarkably, enforcing symmetry in the coupling matrix has little-to-no effect on model performance, while introducing a nonzero self-coupling term has a drastic positive impact even on the symmetric variants. This suggests that the RM, and not just the absence of chaos, is the key feature enabling learning.

This work was supported by the Future Artificial Intelligence Research (FAIR) Foundation. We thank N. Brunel for stimulating discussions.

-
- [1] Y. LeCun, Y. Bengio, and G. Hinton, *nature* **521**, 436 (2015).
 [2] J. Sohl-Dickstein, E. Weiss, N. Maheswaranathan, and

- S. Ganguli, in *International conference on machine learning* (pmlr, 2015) pp. 2256–2265.
 [3] A. Vaswani, N. Shazeer, N. Parmar, J. Uszkoreit, L. Jones, A. N. Gomez, L. Kaiser, and I. Polosukhin, *Advances in neural information processing systems* **30** (2017).
 [4] The new NeuroAI Panel, *Nature Machine Intelligence* **6**, 245 (2024).
 [5] A. Ororbia, A. Mali, A. Kohan, B. Millidge, and T. Salvatori, *arXiv preprint arXiv:2403.18929* (2024).
 [6] T. P. Lillicrap, D. Cownden, D. B. Tweed, and C. J. Akerman, *Nature communications* **7**, 13276 (2016).
 [7] D.-H. Lee, S. Zhang, A. Fischer, and Y. Bengio, in *Joint european conference on machine learning and knowledge discovery in databases* (Springer, 2015) pp. 498–515.
 [8] G. Hinton, *arXiv preprint arXiv:2212.13345* **2**, 5 (2022).
 [9] R. P. Rao and D. H. Ballard, *Nature neuroscience* **2**, 79 (1999).
 [10] B. Scellier and Y. Bengio, *Frontiers in computational neuroscience* **11**, 24 (2017).
 [11] K. Nakajima and I. Fischer, *Reservoir computing* (Springer, 2021).
 [12] J. H. Lee, T. Delbruck, and M. Pfeiffer, *Frontiers in neuroscience* **10**, 508 (2016).
 [13] C. Baldassi, A. Ingrosso, C. Lucibello, L. Saglietti, and R. Zecchina, *Phys. Rev. Lett.* **115**, 128101 (2015).
 [14] M. Stern, H. Sompolinsky, and L. F. Abbott, *Physical Review E* **90**, 062710 (2014).
 [15] J. J. Hopfield, *Proceedings of the national academy of sciences* **79**, 2554 (1982).
 [16] H. Sompolinsky, A. Crisanti, and H.-J. Sommers, *Physical review letters* **61**, 259 (1988).
 [17] C. Baldassi, C. Borgs, J. T. Chayes, A. Ingrosso, C. Lucibello, L. Saglietti, and R. Zecchina, *Proceedings of the National Academy of Sciences* **113**, E7655 (2016).
 [18] C. Baldassi, C. Lauditi, E. M. Malatesta, G. Perugini, and R. Zecchina, *Physical Review Letters* **127**, 278301 (2021).
 [19] D. Barbier, *arXiv preprint arXiv:2505.20954* (2025).
 [20] D. Gamarnik, *Proceedings of the National Academy of Sciences* **118**, e2108492118 (2021).
 [21] D. Badalotti, C. Baldassi, M. Mezard, M. Scardecchia, and R. Zecchina, in preparation (2025).
 [22] C. Baldassi, F. Gerace, H. J. Kappen, C. Lucibello, L. Saglietti, E. Tartaglione, and R. Zecchina, *Physical review letters* **120**, 268103 (2018).
 [23] B. L. Annesi, C. Lauditi, C. Lucibello, E. M. Malatesta, G. Perugini, F. Pittorino, and L. Saglietti, *Physical Review Letters* **131**, 227301 (2023).
 [24] C. Baldassi, F. Pittorino, and R. Zecchina, *Proceedings of the National Academy of Sciences* **117**, 161 (2020).
 [25] H. Jaeger, Bonn, Germany: German National Research Center for Information Technology GMD Technical Report **148** (2001).
 [26] G. Parisi, *Journal of Physics A: Mathematical and General* **13**, 1101 (1980).
 [27] M. Mézard, G. Parisi, and M. A. Virasoro, *Spin-Glass Theory and Beyond* (World Scientific, Singapore, 1987).

SUPPLEMENTARY MATERIAL

The entropy of fixed points

We consider a neural network made of a chain of L core modules. Each core module with $\ell \in \{2, \dots, L-1\}$ is coupled to the module $\ell-1$ and the module $\ell+1$ through a positive couplings $\lambda_L \geq 0$ and $\lambda_R \geq 0$. For the sake of simplicity, in the main text we discussed just the case $\lambda_L = \lambda_R = \lambda$. We are interested in the number of fixed points of the dynamics. Let us denote the local fields at layer ℓ by:

$$h_i^\ell = \sum_j J_{ij}^\ell s_j^\ell \quad (10)$$

$$(11)$$

For $L \geq 2$, the fixed points conditions are expressed as :

$$\begin{aligned} \forall \ell \in \{2, \dots, L-1\} : & \quad s_i^\ell h_i^\ell + J_D + \lambda_L s_i^{\ell-1} s_i^\ell + \lambda_R s_i^\ell s_i^{\ell+1} > 0 \\ \text{For } \ell = 1 : & \quad s_i^\ell h_i^\ell + J_D + \lambda_R s_i^\ell s_i^{\ell+1} > 0 \\ \text{For } \ell = L : & \quad s_i^\ell h_i^\ell + J_D + \lambda_L s_i^\ell s_i^{\ell-1} > 0 \end{aligned} \quad (12)$$

If $L = 1$ there are no λ -couplings and the fixed point condition is just

$$s_i^1 h_i^1 + J_D > 0 \quad (13)$$

The number of fixed points is given by

$$\mathcal{N}_{\text{fp}} = \sum_s \prod_{\ell=1}^{L-1} \prod_{i=1}^N \theta(u_i^\ell(s)) \quad (14)$$

where the \sum_s denotes a sum over all the internal representations $\{s_i^\ell\}$ for $\ell \in \{1, \dots, L\}$, while $u_i^\ell(s)$ are the conditions appearing in Eqs. (12) and (13). The entropy of fixed points is defined as

$$S_{\text{fp}} = \lim_{N \rightarrow \infty} \frac{1}{LN} \log \mathcal{N}_{\text{fp}} \quad (15)$$

Annealed average. We start the study by considering the annealed average of this number of fixed points over the choice of the couplings J^ℓ with their respective Gaussian measures. It proceeds as follows. We first notice that, when averaging over the J , the variables h_i^ℓ are iid Gaussian of mean zero and variance unity. Defining

$$H(x) = \int_x^\infty \frac{dt}{\sqrt{2\pi}} e^{-t^2/2}, \quad (16)$$

the annealed average of the number of fixed points is $\overline{\mathcal{N}}_{\text{fp}} = z^N$ where the partition function z is

$$z = \sum_{s^1, \dots, s^L} H(-J_D - \lambda_R s^1 s^2) \prod_{\ell=2}^{L-1} H(-J_D - \lambda_L s^{\ell-1} s^\ell - \lambda_R s^\ell s^{\ell+1}) H(-J_D - \lambda_L s^{L-1} s^L) \quad (17)$$

This partition function can be computed by transfer matrix. Note that the weight is invariant by flipping all the spins. So we can compute z_+ which is the partition function when we fix $s_1 = 1$ and we have $z = 2z_+$.

Transfer matrix computation: We define the vector

$$f_k(s^k, s^{k+1}) = \sum_{s^1, \dots, s^{k-1}} H(-J_D - \lambda_R s^1 s^2) \prod_{\ell=2}^k H(-J_D - \lambda_L s^{\ell-1} s^\ell - \lambda_R s^\ell s^{\ell+1}) \quad (18)$$

which satisfies the recursion relation

$$f_{k+1}(s^{k+1}, s^{k+2}) = \sum_{s^k} f_k(s^k, s^{k+1}) H(-J_D - \lambda_L s^k s^{k+1} - \lambda_R s^{k+1} s^{k+2}) \quad (19)$$

with the initial condition

$$f_1(s_1, s_2) = H(-J_D - \lambda_R s^1 s^2) \quad (20)$$

We can express the annealed entropy associated with the average number of fixed points as:

$$S_a = \frac{1}{NL} \log \overline{\mathcal{N}_{\text{fp}}} = \frac{1}{L} \log 2 + \frac{1}{L} \log \sum_{s^{L-1}, s^L} f_{L-1}(s^{L-1}, s^L) H(-J_D - \lambda_L s^{L-1} s^L) \quad (21)$$

We introduce a four dimensional vector \vec{f}_k defined as

$$\vec{f}_k = \begin{pmatrix} f_k(-1, -1) \\ f_k(-1, 1) \\ f_k(1, -1) \\ f_k(1, 1) \end{pmatrix}. \quad (22)$$

Then the recursion (19) can be expressed as $\vec{f}_{k+1} = M_{k+1} \vec{f}_k$ where M_{k+1} is the 4×4 matrix:

$$\begin{pmatrix} H_{--} & 0 & H_{+-} & 0 \\ H_{-+} & 0 & H_{++} & 0 \\ 0 & H_{++} & 0 & H_{-+} \\ 0 & H_{+-} & 0 & H_{--} \end{pmatrix} \quad (23)$$

where

$$H_{\tau_1 \tau_2} = H(-J_D + \tau_1 \lambda_L + \tau_2 \lambda_R), \quad (24)$$

with $\tau_1, \tau_2 \in \{\pm 1\}$. The initial vector is

$$\vec{f}_1 = \begin{pmatrix} 0 \\ 0 \\ H(-J_D + \lambda_R) \\ H(-J_D - \lambda_R) \end{pmatrix} \quad (25)$$

The average number of fixed points is given by (21) where $\vec{f}_{L-1} = M^{L-2} \vec{f}_1$. Shallow networks are special cases :

$$L = 1 : \quad \frac{1}{N} \log \overline{\mathcal{N}_{\text{fp}}} = \log 2 + \log H(-J_D) \quad (26)$$

$$L = 2 : \quad \frac{1}{2N} \log \overline{\mathcal{N}_{\text{fp}}} = \frac{1}{2} \log 2 + \frac{1}{2} \log [H(-J_D - \lambda_R) H(-J_D - \lambda_L) + H(-J_D + \lambda_R) H(-J_D + \lambda_L)] \quad (27)$$

The result for $L = 2$ is shown in Fig. 4. Within this annealed approximation, one sees that the use of nonzero values of λ_L, λ_R plays a role similar to J_D in stabilizing fixed points.

Tightness of the annealed average The annealed average that we have just performed approximates the quenched average $\overline{\log \mathcal{N}_{\text{fp}}}$ by its first moment $\log \overline{\mathcal{N}_{\text{fp}}}$. Let us show that, in the $L = 1$ case, this first moment bound is tight. Let's give here a brief account of calculations for the core model ($L = 1$). A detailed discussion in more general cases will be presented in [21].

A configuration \mathbf{s} is a fixed point if $s_i(\sum_{j \neq i} J_{ij} s_j + J_D s_i) = h_i s_i + J_D > 0$ for all i . As discussed above, for fixed \mathbf{s} , we have that the local fields are Gaussian

$$h_i := \sum_{j \neq i} J_{ij} s_j \sim \mathcal{N}\left(0, \frac{N-1}{N}\right),$$

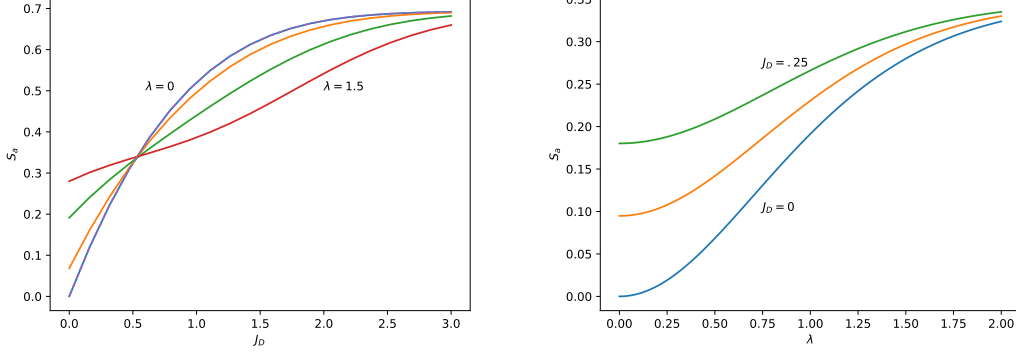


FIG. 4: Annealed entropy S_a of the number of fixed points, in the case of two core modules, $L = 2$, and $\lambda_L = \lambda_R = \lambda$. Left: S_a is plotted versus J_D , for $\lambda = 0, 0.5, 1, 1.5$. Right: S_a is plotted versus λ , for $J_D = 0, 0.125, 0.25$

and the probabilities of satisfying the fixed point conditions are

$$\mathcal{P}(s_i h_i + J_D > 0) = H\left(-\frac{J_D}{\sigma_N}\right),$$

with $\sigma_N^2 = (N-1)/N \rightarrow 1$. Since rows are independent, we have

$$\mathbb{E}[Z] = \sum_{\mathbf{s}} \prod_{i=1}^N H\left(-\frac{J_D}{\sigma_N}\right) = \left(2 H\left(-\frac{J_D}{\sigma_N}\right)\right)^N \xrightarrow{N \rightarrow \infty} (2 H(-J_D))^N. \quad (28)$$

Upon introducing the overlap $q = \frac{1}{N} \sum_i s_i s'_i \in [-1, 1]$ between pairs of configurations s and s' , and summing over q , the averaged second moment of Z can be written as

$$\mathbb{E}[Z^2] = \sum_{k=0}^N 2^N \binom{N}{k} F(J_D, q_k)^k F(J_D, -q_k)^{N-k},$$

where $q_k = \frac{2k-N}{N}$ and

$$F(J_D, x) = \int_{-J_D}^{\infty} \frac{e^{-t^2/2}}{\sqrt{2\pi}} dt H\left(-\frac{xt + J_D}{\sqrt{1-x^2}}\right)$$

To write $\mathbb{E}[Z^2]$ in the limit $N \rightarrow \infty$, we need to solve a saddle point equation. Setting $x = k/N$ and $q = 2x - 1$, $\mathbb{E}[Z^2]$ has a large- N exponent

$$\frac{1}{N} \log \mathbb{E}[Z^2] = \sup_{q \in [-1, 1]} \left\{ \log 2 + H_b\left(\frac{1+q}{2}\right) + \frac{1+q}{2} \log F(J_D, q) + \frac{1-q}{2} \log F(J_D, -q) \right\},$$

where $H_b(p) = -p \log p - (1-p) \log(1-p)$ is the binary entropy. This exponent is even in q and the maximum is attained at $q = 0$. Therefore, to the leading exponential order, one finds:

$$\frac{1}{N} \log \mathbb{E}[Z^2] = 2 \log(2 H(-J_D)) = \frac{2}{N} \log \mathbb{E}[Z].$$

It follows:

$$\frac{\mathbb{E}[Z^2]}{\mathbb{E}[Z]^2} \xrightarrow{N \rightarrow \infty} 1$$

with a vanishing relative variance $\frac{\text{Var}(Z)}{\mathbb{E}[Z]^2} \rightarrow 0$. Hence the annealed estimate $\mathbb{E}[Z] \simeq (2H(-J_D))^N$ is *self-averaging* and gives a tight exponential order bound in the case $L = 1$.

Replica symmetric computation of the entropy of fixed points

A complementary approach consists in computing the entropy of fixed points using the replica method.

General expression

The n -th power of the number of fixed points is given by

$$\overline{\mathcal{N}_{\text{fp}}^n} = \sum_{s_a} \prod_{\ell=1}^L \prod_i \prod_{a=1}^n \theta(u_i^\ell(s_a)) \quad (29)$$

where the \sum_{s_a} denotes a sum over all the internal representations $\{s_{ia}^\ell\}$ for $\ell \in \{1, \dots, L\}$. When sampling the J , the local fields $h_{ia}^\ell = \sum_j J_{ij}^\ell s_{ja}^\ell$ have a joint Gaussian distribution with mean zero. They are independent for each i, ℓ and their covariance in replica space is

$$\mathbb{E}[h_{ia}^\ell h_{jb}^m] = \delta_{ij} \delta^{\ell m} q_{ab}^\ell \quad (30)$$

where

$$q_{ab}^\ell = \frac{1}{N} \sum_j s_{ja}^\ell s_{jb}^\ell. \quad (31)$$

Introducing this replica overlap q_{ab}^ℓ in each layer ℓ and the corresponding Lagrange multiplier \hat{q}_{ab}^ℓ , we find the expression:

$$\begin{aligned} \overline{\mathcal{N}_{\text{fp}}^n} = & \sum_s \int \prod_{a < b} dq_{ab} d\hat{q}_{ab} e^{-N \sum_\ell \sum_{a < b} \hat{q}_{ab}^\ell q_{ab}^\ell + \sum_{\ell, i, a, b} \hat{q}_{ab}^\ell s_{ia}^\ell s_{ib}^\ell} \\ & \prod_{i\ell} \left[\mathbb{E}_{\{h_a\} \sim \mathcal{N}(0, q_{ab}^\ell)} \prod_{a=1}^n \theta(s_{ia}^\ell h_a + J_D + \lambda_L s_{ia}^{\ell-1} s_{ia}^\ell + \lambda_R s_{ia}^\ell s_{ia}^{\ell+1}) \right] \end{aligned} \quad (32)$$

where the product over ℓ runs from $\ell = 1$ to $\ell = L$, and it is understood that the term $\lambda_L s_{ia}^{\ell-1} s_{ia}^\ell$ is absent when $\ell = 1$, and the term $\lambda_R s_{ia}^\ell s_{ia}^{\ell+1}$ is absent when $\ell = L$.

We need to compute the expectation over the gaussian fields h_a . Let us denote by $\mathcal{P}_q(\{v_a, s_a\})$ the probability that the Gaussian variables h_1, \dots, h_n with mean zero and covariance matrix q satisfy the constraints $\forall a : s_a h_a + v_a > 0$. Then

$$\begin{aligned} \overline{\mathcal{N}_{\text{fp}}^n} = & \int \prod_{a < b} dq_{ab} d\hat{q}_{ab} e^{-N \sum_\ell \sum_{a < b} \hat{q}_{ab}^\ell q_{ab}^\ell} \\ & \prod_i \left[\sum_{\{s_a^\ell\}} e^{\sum_{\ell, a < b} \hat{q}_{ab}^\ell s_a^\ell s_b^\ell} \prod_{\ell=1}^{L-1} \mathcal{P}_{q^\ell + \Delta\pi_n}(\{J_D + \lambda_L s_a^{\ell-1} s_a^\ell + \lambda_R s_a^\ell s_a^{\ell+1}, s_a^\ell\}) \right] \end{aligned} \quad (33)$$

We now look at a replica symmetric Ansatz for the overlap matrices q_{ab}^ℓ , defined by

$$q_{aa}^\ell = 1 \quad ; \quad q_{ab}^\ell = q^\ell \quad \text{for } a \neq b \quad (34)$$

and same for \hat{q} .

Given $q^\ell = q$, we can write the joint density of $\tilde{h}_1, \dots, \tilde{h}_n$ as

$$P(\tilde{h}_1, \dots, \tilde{h}_n) = \int \frac{dz}{\sqrt{2\pi q}} e^{-z^2/(2q)} \prod_{a=1}^n \left[\frac{1}{\sqrt{2\pi(1-q)}} e^{-(\tilde{h}_a - z)^2/(2(1-q))} \right] \quad (35)$$

Therefore the function $\mathcal{P}_q(\{v_a, s_a\})$ can be easily computed:

$$\mathcal{P}_q(\{v_a, s_a\}) = \int dh_1 \dots dh_n P(h_1, \dots, h_n) \prod_{a=1}^n \theta(h_a s_a + v_a) = \int Dz \prod_{a=1}^n H\left(\frac{-v_a - s_a z \sqrt{q}}{\sqrt{1-q}}\right) \quad (36)$$

In our case we have, in layer ℓ , $v_a^\ell = J_D + \lambda_L s_a^{\ell-1} s_a^\ell + \lambda_R s_a^\ell s_a^{\ell+1}$.

Using

$$e^{\sum_{a < b} \hat{q}_{ab} s_a^\ell s_b^\ell} = e^{-n\hat{q}^\ell/2} \int Dt^\ell e^{\sqrt{\hat{q}^\ell} t^\ell \sum_a s_a^\ell} \quad (37)$$

we get

$$\overline{\mathcal{N}}_{\text{fp}}^n = \text{Extr}_{\{\hat{q}^\ell, q^\ell\}} e^{\frac{Nn}{2} \sum_\ell \hat{q}^\ell (q^\ell - 1)} \prod_i \left[\int \prod_{\ell=1}^L Dt^\ell Dz^\ell \left(\sum_{s^1, \dots, s^L} e^{\sum_\ell \sqrt{\hat{q}^\ell} t^\ell s^\ell} \prod_\ell H \left(\frac{-J_D - \lambda_L s^{\ell-1} s^\ell - \lambda_R s^\ell s^{\ell+1} - s^\ell z^\ell \sqrt{q^\ell}}{\sqrt{1 - q^\ell}} \right) \right)^n \right] \quad (38)$$

This gives finally

$$\frac{1}{NL} \log \overline{\mathcal{N}}^n = \frac{1}{L} \text{Extr}_{\{\hat{q}^\ell, q^\ell\}} \left[\frac{1}{2} \sum_\ell \hat{q}^\ell (q^\ell - 1) + \varphi(\{\hat{q}^\ell, q^\ell\}) \right] \quad (39)$$

where

$$\varphi(\{\hat{q}^\ell, q^\ell\}) = \int \prod_{\ell=1}^L Dt^\ell Dz^\ell \log (\zeta(\{\hat{q}^\ell, q^\ell, z^\ell, t^\ell\})) \quad (40)$$

and

$$\zeta(\{\hat{q}^\ell, q^\ell, z^\ell, t^\ell\}) = \sum_{s^1, \dots, s^L} e^{\sum_\ell \sqrt{\hat{q}^\ell} t^\ell s^\ell} \prod_{\ell=1}^{L-1} H \left(\frac{-J_D - \lambda_L s^{\ell-1} s^\ell - \lambda_R s^\ell s^{\ell+1} - s^\ell z^\ell \sqrt{q^\ell}}{\sqrt{1 - q^\ell}} \right) \quad (41)$$

We see that ζ is a partition functions of an Ising chain with next-nearest neighbor interactions, with gaussian external fields t^ℓ and z^ℓ , and the quantities $\langle s^\ell \rangle^2$ are the Edwards Anderson order parameter for the spins in layer ℓ . So all this can be studied numerically adapting the transfer matrix already introduced in computation of the annealed average. Let us focus here on the cases $L = 1, 2$ which can be handled directly. We get:

Case L=1:

$$\zeta(\{\hat{q}^1, q^1, z^1, t^1\}) = e^{\sqrt{\hat{q}^1} t^1} H \left(\frac{-J_D - z^1 \sqrt{q^1 + \Delta}}{\sqrt{1 - q^1}} \right) + e^{-\sqrt{\hat{q}^1} t^1} H \left(\frac{-J_D + z^1 \sqrt{q^1 + \Delta}}{\sqrt{1 - q^1}} \right) \quad (42)$$

Case L=2:

$$\begin{aligned} \zeta(\{\hat{q}^1, q^1, z^1, t^1, \hat{q}^2, q^2, z^2, t^2\}) = & \\ & e^{-\sqrt{\hat{q}^1} t^1 - \sqrt{\hat{q}^2} t^2} H \left(\frac{-J_D - \lambda_R + z^1 \sqrt{q^1 + \Delta}}{\sqrt{1 - q^1}} \right) H \left(\frac{-J_D - \lambda_L + z^2 \sqrt{q^2 + \Delta}}{\sqrt{1 - q^2}} \right) \\ & + e^{-\sqrt{\hat{q}^1} t^1 + \sqrt{\hat{q}^2} t^2} H \left(\frac{-J_D / \lambda_R + z^1 \sqrt{q^1 + \Delta}}{\sqrt{1 - q^1}} \right) H \left(\frac{-J_D + \lambda_L - z^2 \sqrt{q^2 + \Delta}}{\sqrt{1 - q^2}} \right) \\ & + e^{\sqrt{\hat{q}^1} t^1 - \sqrt{\hat{q}^2} t^2} H \left(\frac{-J_D + \lambda_R - z^1 \sqrt{q^1 + \Delta}}{\sqrt{1 - q^1}} \right) H \left(\frac{-J_D + \lambda_L + z^2 \sqrt{q^2 + \Delta}}{\sqrt{1 - q^2}} \right) \\ & + e^{\sqrt{\hat{q}^1} t^1 + \sqrt{\hat{q}^2} t^2} H \left(\frac{-J_D - \lambda_R - z^1 \sqrt{q^1 + \Delta}}{\sqrt{1 - q^1}} \right) H \left(\frac{-J_D - \lambda_L - z^2 \sqrt{q^2 + \Delta}}{\sqrt{1 - q^2}} \right) \end{aligned} \quad (43)$$

Using these expressions, we can study in detail the replica symmetric result for the number of fixed points.

Detailed RS study for a single core module, $L = 1$

The quenched evaluation with replica symmetric Ansatz gives:

$$S_{rs} = \frac{1}{N} \log \overline{\mathcal{N}} = \text{Extr}_{\{\hat{q}, q\}} \left[\frac{1}{2} \hat{q} (q - 1) + \int Dt Dz \log \zeta(\hat{q}, q, z, t) \right] \quad (44)$$

where

$$\zeta(\{\hat{q}, q, z, t\}) = e^{\sqrt{\hat{q}}t} H\left(\frac{-J_D - z\sqrt{q}}{\sqrt{1-q}}\right) + e^{-\sqrt{\hat{q}}t} H\left(\frac{-J_D + z\sqrt{q}}{\sqrt{1-q}}\right) \quad (45)$$

This has a saddle point at $q = \hat{q} = 0$, for which $\zeta = 2H(-J_D)$, giving back the annealed average.

In order to check the stability of this saddle point, let us expand S_{rs} to second order in powers of q, \hat{q} . We obtain:

$$\begin{aligned} S_{rs}^{(2)} = & \frac{1}{2}\hat{q}(q-1) + \log[2H(-J_D)] + \frac{1}{2}\hat{q} \\ & - \frac{1}{4}\hat{q}^2 - \hat{q}q \frac{e^{-J_D^2}}{4\pi H(-J_D)^2} - q^2 \frac{J_D^2 e^{-J_D^2}}{8\pi H(-J_D)^2} \end{aligned} \quad (46)$$

This is a concave function of \hat{q} , with a minimum at

$$\hat{q} = q \frac{-2e^{-J_D^2} + 4\pi H(-J_D)^2}{4\pi H(-J_D)^2} \quad (47)$$

Evaluating $S_{rs}^{(2)}$ at this value of \hat{q} we obtain

$$S_{rs}^{(2)} = \log[2H(-J_D)] + \left(\frac{1}{4} + \frac{e^{-2J_D^2}}{16\pi^2 H(-J_D)^4}\right) - \frac{(2 + J_D^2)e^{-J_D^2}}{8\pi H(-J_D)^2} \quad (48)$$

which is a convex function of q with minimum at $q = 0$, for all $J_D \geq -.178$ (See Fig.5). This shows that the saddle point at $q = \hat{q} = 0$ is stable. We have not found any other saddle point. This confirms that the annealed average expression for the entropy of fixed points is exact.

Detailed RS study for $L = 2$

Taking $\Delta_V = \Delta_W = 0$, we had found the annealed result:

$$\begin{aligned} \frac{1}{2N} \log \overline{\mathcal{N}_{\text{fp}}} = & \frac{1}{2} \log 2 + \frac{1}{2} \log [H(-J_D - \lambda_R) H(-J_D - \lambda_L) + \\ & H(-J_D + \lambda_R) H(-J_D + \lambda_L)] \end{aligned} \quad (49)$$

Assuming that by symmetry the order parameters q, \hat{q} are the same in each of the two layers, the quenched evaluation with replica symmetric Ansatz gives (see 38):

$$S_{rs} = \frac{1}{2N} \log \overline{\mathcal{N}} = \frac{1}{2} \text{Extr}_{\{\hat{q}, q\}} \left[\hat{q}(q-1) + \int Dt_1 Dz_1 Dt_2 Dz_2 \log \zeta(\hat{q}, q, z_1, t_1, z_2, t_2) \right] \quad (50)$$

where

$$\begin{aligned} \zeta(\{\hat{q}, q, z_1, t_1, z_2, t_2\}) = & \\ & e^{\sqrt{\hat{q}}(-t_1-t_2)} H\left(\frac{-J_D - \lambda_R + z_1\sqrt{q}}{\sqrt{1-q}}\right) H\left(\frac{-J_D - \lambda_L + z_2\sqrt{q}}{\sqrt{1-q}}\right) \\ & + e^{\sqrt{\hat{q}}(-t_1+t_2)} H\left(\frac{-J_D + \lambda_R + z_1\sqrt{q}}{\sqrt{1-q}}\right) H\left(\frac{-J_D + \lambda_L - z_2\sqrt{q}}{\sqrt{1-q}}\right) \\ & + e^{\sqrt{\hat{q}}(t_1-t_2)} H\left(\frac{-J_D + \lambda_R - z_1\sqrt{q}}{\sqrt{1-q}}\right) H\left(\frac{-J_D + \lambda_L + z_2\sqrt{q}}{\sqrt{1-q}}\right) \\ & + e^{\sqrt{\hat{q}}(t_1+t_2)} H\left(\frac{-J_D - \lambda_R - z_1\sqrt{q}}{\sqrt{1-q}}\right) H\left(\frac{-J_D - \lambda_L - z_2\sqrt{q}}{\sqrt{1-q}}\right) \end{aligned} \quad (51)$$

In order to check the stability of the saddle point at $q = \hat{q} = 0$, we proceed as for the case $L = 2$: we expand S_{rs} to second order in powers of q, \hat{q} , find the saddle point value of \hat{q} and substitute it into the expansion. Specializing to the case $\lambda_L = \lambda_R = \lambda$, the resulting quadratic form in q is given by

$$\begin{aligned} S_{rs}^{(2)} = & \frac{1}{2} [\log 2 + \log(H(-J_D - \lambda)^2 + H(-J_D + \lambda)^2)] \\ & + \frac{A(J_D, \lambda)}{B(J_D, \lambda)} q^2 \end{aligned} \quad (52)$$

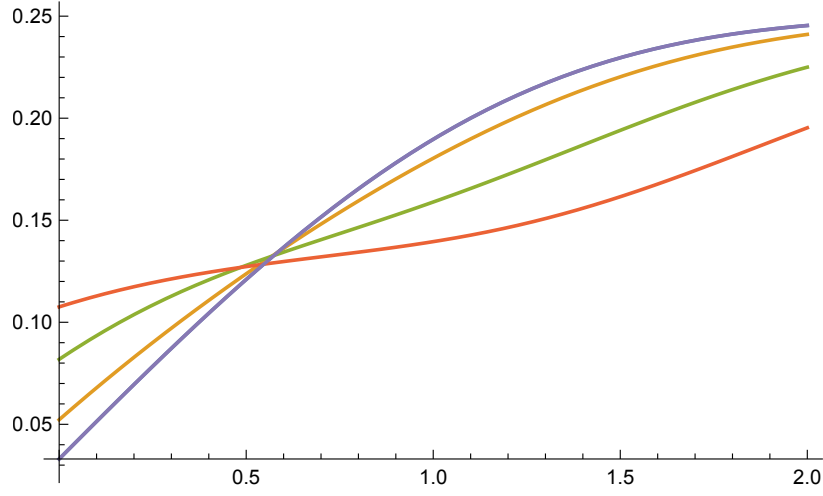


FIG. 5: In the case with two core modules, $L = 2$, we plot the coefficient of q^2 in the quadratic expansion of the RS free entropy. This coefficient is plotted versus J_D for $\lambda = 0, 0.5, 1, 1.5$, from top to bottom on the right part of the figure (at $J_D = 2$). The top blue curve with $\lambda = 0$ is the same result as for $L = 1$. The coefficient is positive for all values of J_D, λ of interest. This shows that the RS saddle point at $q = \hat{q} = 0$ is locally stable.

where

$$\begin{aligned}
A(J_D, \lambda) = & 2\pi^2 H(-J_D - \lambda)^8 + 8\pi^2 H(\lambda - J_D)^2 H(-J_D - \lambda)^6 - 4e^{-(J_D + \lambda)^2} \pi H(-J_D - \lambda)^6 \\
& - 2e^{-(J_D + \lambda)^2} J_D^2 \pi H(-J_D - \lambda)^6 - 2e^{-(J_D + \lambda)^2} \lambda^2 \pi H(-J_D - \lambda)^6 \\
& - 4e^{-(J_D + \lambda)^2} J_D \lambda \pi H(-J_D - \lambda)^6 - 4e^{3J_D^2 + 8\lambda J_D + 3\lambda^2 - 4(J_D + \lambda)^2} J_D^2 \pi H(\lambda - J_D) H(-J_D - \lambda)^5 \\
& + 4e^{3J_D^2 + 8\lambda J_D + 3\lambda^2 - 4(J_D + \lambda)^2} \lambda^2 \pi H(\lambda - J_D) H(-J_D - \lambda)^5 + e^{-2(J_D + \lambda)^2} H(-J_D - \lambda)^4 \\
& + 2e^{4J_D \lambda - 2(J_D + \lambda)^2} H(-J_D - \lambda)^4 - e^{8J_D \lambda - 2(J_D + \lambda)^2} H(-J_D - \lambda)^4 + 12\pi^2 H(\lambda - J_D)^4 H(-J_D - \lambda)^4 \\
& - 8e^{-(J_D + \lambda)^2} \pi H(\lambda - J_D)^2 H(-J_D - \lambda)^4 - 4e^{4J_D \lambda - (J_D + \lambda)^2} \pi H(\lambda - J_D)^2 H(-J_D - \lambda)^4 \\
& - 2e^{4J_D \lambda - (J_D + \lambda)^2} J_D^2 \pi H(\lambda - J_D)^2 H(-J_D - \lambda)^4 - 2e^{4J_D \lambda - (J_D + \lambda)^2} \lambda^2 \pi H(\lambda - J_D)^2 H(-J_D - \lambda)^4 \\
& + 4e^{4J_D \lambda - (J_D + \lambda)^2} J_D \lambda \pi H(\lambda - J_D)^2 H(-J_D - \lambda)^4 + 8\pi^2 H(\lambda - J_D)^6 H(-J_D - \lambda)^2 \\
& - 4e^{-(J_D + \lambda)^2} \pi H(\lambda - J_D)^4 H(-J_D - \lambda)^2 - 8e^{4J_D \lambda - (J_D + \lambda)^2} \pi H(\lambda - J_D)^4 H(-J_D - \lambda)^2 \\
& - 2e^{-(J_D + \lambda)^2} J_D^2 \pi H(\lambda - J_D)^4 H(-J_D - \lambda)^2 - 2e^{-(J_D + \lambda)^2} \lambda^2 \pi H(\lambda - J_D)^4 H(-J_D - \lambda)^2 \\
& - 4e^{-(J_D + \lambda)^2} J_D \lambda \pi H(\lambda - J_D)^4 H(-J_D - \lambda)^2 + 4e^{2(J_D^2 + 4\lambda J_D + \lambda^2) - 4(J_D + \lambda)^2} H(\lambda - J_D)^2 H(-J_D - \lambda)^2 \\
& - 4e^{3J_D^2 + 8\lambda J_D + 3\lambda^2 - 4(J_D + \lambda)^2} J_D^2 \pi H(\lambda - J_D)^5 H(-J_D - \lambda) \\
& + 4e^{3J_D^2 + 8\lambda J_D + 3\lambda^2 - 4(J_D + \lambda)^2} \lambda^2 \pi H(\lambda - J_D)^5 H(-J_D - \lambda) + 2\pi^2 H(\lambda - J_D)^8 \\
& - 4e^{J_D^2 + 6\lambda J_D + \lambda^2 - 2(J_D + \lambda)^2} \pi H(\lambda - J_D)^6 - 2e^{J_D^2 + 6\lambda J_D + \lambda^2 - 2(J_D + \lambda)^2} J_D^2 \pi H(\lambda - J_D)^6 \\
& - 2e^{J_D^2 + 6\lambda J_D + \lambda^2 - 2(J_D + \lambda)^2} \lambda^2 \pi H(\lambda - J_D)^6 + 4e^{J_D^2 + 6\lambda J_D + \lambda^2 - 2(J_D + \lambda)^2} J_D \lambda \pi H(\lambda - J_D)^6 \\
& - e^{-2(J_D + \lambda)^2} H(\lambda - J_D)^4 + 2e^{4J_D \lambda - 2(J_D + \lambda)^2} H(\lambda - J_D)^4 + e^{8J_D \lambda - 2(J_D + \lambda)^2} H(\lambda - J_D)^4
\end{aligned} \tag{53}$$

and

$$B(J_D, \lambda) = 16\pi^2 (H(-J_D - \lambda)^2 + H(\lambda - J_D)^2)^2 (H(-J_D - \lambda)^4 + H(\lambda - J_D)^4) \tag{54}$$

Fig. 5 shows that the ratio $A(J_D, \lambda)/B(J_D, \lambda)$ is always positive in the ranges of J_D, λ of interest. This shows that the saddle point at $q = \hat{q} = 0$ is locally stable, which indicates that the annealed result for the entropy of fixed points is correct also for this case with $L = 2$.

Local Entropy

Here we derive the expression for the free-energy density $\Phi(d, y)$ within the local entropy approach. We follow ref. [13] and derive the local entropy theory through a 1-RSB formalism. We want to compute the number of fixed points $\mathcal{N}(\tilde{s}, d)$ at distance d from an optimal reference configuration \tilde{s} . We adopt the short notation \mathcal{N} for $\mathcal{N}(\tilde{s}, y)$ and Φ for $\Phi(d, y)$. We study the quenched average of $\log \mathcal{N}$ with respect to the choice the internal couplings in each module, using n replicas, for a generic multilayer model consisting of L layers of core modules. The n -th power of \mathcal{N} is expressed as:

$$\mathcal{N}^n = \sum_s \prod_{\ell=1}^L \prod_{i=1}^N \prod_{a=1}^n \theta(s_{ia}^\ell h_i^\ell + J_D + \lambda s_{ia}^{\ell-1} s_{ia}^\ell + \lambda s_{ia}^\ell s_{ia}^{\ell+1}) \quad (55)$$

where the index $\ell \in \{1, \dots, L\}$ denotes the layer, the index $i \in \{1, \dots, N\}$ denotes the neuron within each layer, the index $a \in \{1, \dots, n\}$ is a replica index, the \sum_{s_a} denotes a sum over all the 2^{LNn} internal representations of the variables s_{ia}^ℓ , and θ is Heavyside's step function.

When sampling the J internal to each module to perform the quenched average, the local fields $h_{ia}^\ell = \sum_j J_{ij}^\ell s_{ja}^\ell$ have a joint Gaussian distribution with mean zero. They are independent for each i, ℓ and their covariance in replica space is

$$\mathbb{E} h_{ia}^\ell h_{jb}^m = \delta_{ij} \delta^{\ell m} q_{ab}^\ell \quad (56)$$

where

$$q_{ab}^\ell = \frac{1}{N} \sum_j s_{ja}^\ell s_{jb}^\ell \quad (57)$$

Introducing this replica overlap q_{ab}^ℓ in each layer ℓ and the corresponding Lagrange multiplier \hat{q}_{ab}^ℓ , we find the expression:

$$\begin{aligned} \overline{\mathcal{N}^n} = \sum_s \int \prod_{l=1}^L \prod_{a < b} \frac{dq_{ab}^\ell d\hat{q}_{ab}^\ell}{2\pi} e^{-N \sum_\ell \sum_{a < b} \hat{q}_{ab}^\ell q_{ab}^\ell + \sum_{\ell, i, a, b} \hat{q}_{ab}^\ell s_{ia}^\ell s_{ib}^\ell} \\ \prod_{i\ell} \left[\mathbb{E}_{\{h_a\} \sim \mathcal{N}(0, q_{ab}^\ell)} \prod_{a=1}^n \theta(s_{ia}^\ell h_a + J_D + \lambda s_{ia}^{\ell-1} s_{ia}^\ell + \lambda s_{ia}^\ell s_{ia}^{\ell+1}) \right] \end{aligned} \quad (58)$$

where the integrals over the \hat{q} variables run along the imaginary axis.

Let us denote by $\mathcal{P}_q(\{v_a, s_a\})$ the probability that the Gaussian variables h_1, \dots, h_n with mean zero and covariance matrix q satisfy the constraints $\forall a : s_a h_a + v_a > 0$. This is the quantity which appears in the last line of (58).

Let us assume that each q^ℓ matrix has a 1-RSB structure [26, 27] with diagonal equal to 1, elements q_1 inside blocks of size m and elements q_0 outside of the diagonal blocks. Then we can compute the explicit form of $\mathcal{P}_q(\{v_a, s_a\})$. We first write the joint density of h_1, \dots, h_n as:

$$\begin{aligned} P(h_1, \dots, h_n) = \int \frac{dz_0}{\sqrt{2\pi(q_0)}} e^{-z_0^2/(2q_0)} \\ \prod_{B=1}^{n/m} \left(\int \frac{dz_B}{\sqrt{2\pi(q_1 - q_0)}} e^{-(z_B - z_0)^2/(2(q_1 - q_0))} \prod_{a \in B} \left[\frac{1}{\sqrt{2\pi(1 - q_1)}} e^{-(h_a - z_B)^2/(2(1 - q_1))} \right] \right) \end{aligned} \quad (59)$$

where the index B runs over the various blocks of the 1-RSB Ansatz, and in each block the index a can take m values. From this expression we deduce that, when q is a 1-RSB matrix with parameters $q_0, q_1, 1$, one has:

$$\mathcal{P}_q(\{v_a, s_a\}) = \int D_{q_0}(z_0) \prod_{B=1}^{n/m} \left(\int D_{q_1 - q_0}(z_B - z_0) \prod_{a \in B} H\left(\frac{-v_a - z_B s_a}{\sqrt{1 - q_1}}\right) \right), \quad (60)$$

where we use the notation:

$$D_q(z) = \frac{dz}{\sqrt{2\pi q}} e^{-z^2/(2q)} ; \quad H(x) = \int_x^\infty D_1(z) = \frac{1}{2} \text{Erfc}\left(\frac{x}{\sqrt{2}}\right) \quad (61)$$

Then we have

$$\overline{\mathcal{N}^n} = \int \prod_{a < b} dq_{ab}^\ell d\hat{q}_{ab}^\ell e^{-N \sum_\ell \sum_{a < b} \hat{q}_{ab}^\ell q_{ab}^\ell} Z(q, \hat{q})^N \quad (62)$$

where

$$Z(q, \hat{q}) = \sum_{\{s_a^\ell\}} e^{\sum_{\ell, a < b} \hat{q}_{ab}^\ell s_a^\ell s_b^\ell} \prod_{\ell=1}^L \mathcal{P}_{q^\ell}(\{J_D + \lambda s_a^{\ell-1} s_a^\ell + \lambda s_a^\ell s_a^{\ell+1}, s_a^\ell\}) \quad (63)$$

$$= \sum_{\{s_a^\ell\}} e^{\sum_{\ell, a < b} \hat{q}_{ab}^\ell s_a^\ell s_b^\ell} \prod_{\ell=1}^L \int D_{q_0^\ell}(z_0^\ell) \prod_B \left(\int D_{q_1^\ell - q_0^\ell}(z_B^\ell - z_0^\ell) \right. \\ \left. \prod_{a \in B} H \left(\frac{-(J_D + \lambda s_a^{\ell-1} s_a^\ell + \lambda s_a^\ell s_a^{\ell+1} + z_B^\ell s_a^\ell)}{\sqrt{1 - q_1^\ell}} \right) \right) \quad (64)$$

When the \hat{q}^ℓ matrices have a 1-RSB structure with elements \hat{q}_1^ℓ inside blocks of size m and elements \hat{q}_0 outside of the diagonal blocks, we can write

$$e^{\sum_{a < b} \hat{q}_{ab}^\ell s_a^\ell s_b^\ell} = e^{-n \hat{q}_1/2} \int D_{\hat{q}_0^\ell}(t_0^\ell) \prod_B \left[\int D_{\hat{q}_1^\ell - \hat{q}_0^\ell}(t_B^\ell - t_0^\ell) e^{t_B^\ell \sum_{a \in B} s_a^\ell} \right] \quad (65)$$

so that

$$Z(q, \hat{q}) = \prod_{\ell=1}^L \left[\int D_{q_0^\ell}(z_0^\ell) \int D_{\hat{q}_0^\ell}(t_0^\ell) \prod_B \left(\int D_{q_1^\ell - q_0^\ell}(z_B^\ell - z_0^\ell) \int D_{\hat{q}_1^\ell - \hat{q}_0^\ell}(t_B^\ell - t_0^\ell) \right) \right] \\ e^{-(n/2) \sum_\ell \hat{q}_1^\ell} \sum_{\{s_a^\ell\}} e^{\sum_{\ell, a} s_a^\ell t_{B(a)}^\ell} \prod_{\ell, a} H \left(\frac{-(J_D + \lambda_L s_a^{\ell-1} s_a^\ell + \lambda_R s_a^{\ell+1} s_a^\ell + z_B^\ell s_a^\ell)}{\sqrt{1 - q_1^\ell}} \right) \quad (66)$$

We now analyze the core module and the two layer chain.

Core module

Let us specialize first to the case $L = 1$, which corresponds to the bare core module. We find:

$$Z(q, \hat{q}) = \int D_{q_0}(z_0) \int D_{\hat{q}_0}(t_0) \prod_B \left(\int D_{q_1 - q_0}(z_B - z_0) \int D_{\hat{q}_1 - \hat{q}_0}(t_B - t_0) \right) \\ e^{-n \hat{q}_1/2} \sum_{\{s_a\}} e^{\sum_a s_a t_{B(a)}} \prod_a H \left(-\frac{J_D + z_{B(a)} s_a}{\sqrt{1 - q_1}} \right) \quad (67)$$

$$(68)$$

and therefore, in the $n \rightarrow 0$ limit:

$$\log Z = -\frac{n}{2} \hat{q}_1 + \frac{n}{m} \int D_{q_0}(z_0) \int D_{\hat{q}_0}(t_0) \log \left(\int D_{q_1 - q_0}(z_1 - z_0) \int D_{\hat{q}_1 - \hat{q}_0}(t_1 - t_0) \right. \\ \left. \left[e^{t_1} H \left(-\frac{J_D + z_1}{\sqrt{1 - q_1}} \right) + e^{-t_1} H \left(-\frac{J_D - z_1}{\sqrt{1 - q_1}} \right) \right]^m \right) \quad (69)$$

The final result for the free-energy density at fixed $q_1 = 1 - 2d$ and $m = y$ is

$$-y\Phi(y) = \frac{1}{N} \log \overline{\mathcal{N}} = \text{Extr}_{\hat{q}_1, \hat{q}_0, q_0} \left[-\frac{1}{2} \hat{q}_1 + \frac{y}{2} \hat{q}_0 q_0 + \frac{1-y}{2} \hat{q}_1 q_1 \right] \\ + \frac{1}{y} \int D_{q_0}(z_0) \int D_{\hat{q}_0}(t_0) \log \left(\int D_{q_1 - q_0}(z_1 - z_0) \int D_{\hat{q}_1 - \hat{q}_0}(t_1 - t_0) \right. \\ \left. \left[e^{t_1} H \left(-\frac{J_D + z_1}{\sqrt{1 - q_1}} \right) + e^{-t_1} H \left(-\frac{J_D - z_1}{\sqrt{1 - q_1}} \right) \right]^y \right) \quad (70)$$

It can be rewritten as

$$\begin{aligned}
-y\Phi(y) = & \text{Extr}_{\hat{q}_1, \hat{q}_0, q_0} \left[-\frac{1}{2}(\hat{q}_1 - \hat{q}_0 + \hat{q}_0) + \frac{y}{2}\hat{q}_0 q_0 \right. \\
& + \frac{1-y}{2}((\hat{q}_1 - \hat{q}_0)(q_1 - q_0) + (\hat{q}_1 - \hat{q}_0)q_0 + \hat{q}_0(q_1 - q_0) + \hat{q}_0 q_0) \\
& \left. + \frac{1}{y} \int Dz_0 Dt_0 \log \left(\int Dz_1 Dt_1 \left[\sum_s e^{sX} H \left(-\frac{J_D + sY}{\sqrt{1-q_1}} \right) \right]^y \right) \right]
\end{aligned} \tag{71}$$

where:

$$X = t_0 \sqrt{\hat{q}_0} + t_1 \sqrt{\hat{q}_1 - \hat{q}_0} \tag{72}$$

$$Y = z_0 \sqrt{q_0} + z_1 \sqrt{q_1 - q_0} \tag{73}$$

We need to compute the saddle point over q_0 , \hat{q}_0 and \hat{q}_1 . It is clear that the stationnarity equations with respect to q_0 and \hat{q}_0 have the solution $q_0 = \hat{q}_0 = 0$ which correspond to the symmetry of our measure by flipping simultaneously all the fields. We shall assume that this symmetry is not broken. Then we get:

$$-y\Phi(y) = -\frac{1}{2}\hat{q}_1 + \frac{1-y}{2}\hat{q}_1 q_1 + \frac{1}{y} \log \left(\int Dz Dt \left[\sum_s e^{st\sqrt{\hat{q}_1}} H \left(-\frac{J_D + sz\sqrt{\hat{q}_1}}{\sqrt{1-q_1}} \right) \right]^y \right) \tag{74}$$

where \hat{q}_1 is the solution of the stationnarity equation

$$q_1 = \frac{\int Dz Dt \left[\sum_s s e^{st\sqrt{\hat{q}_1}} H \left(-\frac{J_D + sz\sqrt{\hat{q}_1}}{\sqrt{1-q_1}} \right) \right]^2 \left[\sum_s e^{st\sqrt{\hat{q}_1}} H \left(-\frac{J_D + sz\sqrt{\hat{q}_1}}{\sqrt{1-q_1}} \right) \right]^{y-2}}{\int Dz Dt \left[\sum_s e^{st\sqrt{\hat{q}_1}} H \left(-\frac{J_D + sz\sqrt{\hat{q}_1}}{\sqrt{1-q_1}} \right) \right]^y} \tag{75}$$

Two-layer chain

We go back to the general expression (66) and specialize to the case $L = 2$. Using the symmetry between the two layers, it is reasonable to assume that $q_0^1 = q_0^2 = q_0$, $q_1^1 = q_1^2 = q_1$ and similarly for the \hat{q} elements. At the saddle point $q_0 = \hat{q}_0 = 0$, we get

$$\begin{aligned}
-y\Phi(d, y) = & -\hat{q}_1 + (1-y)\hat{q}_1 q_1 + \frac{1}{y} \log \left(\int Dz Dz' Dt Dt' \right. \\
& \left. \left[\sum_{s, s'} e^{\sqrt{\hat{q}_1}(st+s't')} H \left(\frac{-J_D + \lambda ss' - s\sqrt{\hat{q}_1}z}{\sqrt{1-q_1}} \right) H \left(\frac{-J_D + \lambda ss' - s'\sqrt{\hat{q}_1}z'}{\sqrt{1-q_1}} \right) \right]^m \right)
\end{aligned} \tag{76}$$

Where \hat{q}_1 is the solution of the stationarity equation:

$$q_1 = \frac{\int Dz Dz' Dt Dt' \left[\sum_{s, s'} s e^{\sqrt{\hat{q}_1}(st+s't')} H_{ss'}^{(2)} \right]^2 \left[\sum_{s, s'} e^{\sqrt{\hat{q}_1}(st+s't')} H_{ss'}^{(2)} \right]^{m-2}}{\int Dz Dz' Dt Dt' \left[\sum_{s, s'} e^{\sqrt{\hat{q}_1}(st+s't')} H_{ss'}^{(2)} \right]^m} \tag{77}$$

where

$$H_{ss'}^{(2)} = H \left(\frac{-J_D + \lambda ss' - s\sqrt{\hat{q}_1}z}{\sqrt{1-q_1}} \right) H \left(\frac{-J_D + \lambda ss' - s'\sqrt{\hat{q}_1}z'}{\sqrt{1-q_1}} \right) \tag{78}$$

Training schemes

In this section, we discuss some extensions of the training procedure described in the main text, summarized at a high level in Algorithm 1.

Algorithm 1: General Supervised Learning Protocol for Recurrent Neural Networks

Require : Training set $\{(x^\mu, y^\mu)\}_{\mu=1}^P$; initial weights $J \in \mathbb{R}^{N \times N}$, $W^{in} \in \mathbb{R}^{N \times D}$, $W^{out} \in \mathbb{R}^{C \times N}$; class prototypes $W^{back} \in \mathbb{R}^{N \times C}$; adjacency $A \in \{0, 1\}^{N \times N}$; binary vectors $a^{in}, a^{back}, a^{out} \in \{0, 1\}^N$; learning rate η ; margin κ ; external field strengths $\lambda = (\lambda_x, \lambda_y)$.

Ensure : Updated synaptic weights J, W^{in} ; updated readout weights W^{out} .

$\lambda_{\rightarrow} \leftarrow (\lambda_x, 0)$;
for $\mu \leftarrow 1$ **to** P **do**
 $s \leftarrow 0$;
 $s' \leftarrow \text{EvolveUntilConvergence}(s, J, x^\mu, y^\mu, \lambda)$; // Synchronous evolution (Eq. 79)
 $s^* \leftarrow \text{EvolveUntilConvergence}(s', J, x^\mu, 0, \lambda_{\rightarrow})$; // Synchronous evolution (Eq. 79)
 $J, W^{in} \leftarrow \text{UpdateSynapticWeights}(J, W^{in}, s^*, x^\mu, \eta, \kappa)$; // Synaptic plasticity (Eqs. 80--82)
 $W^{out} \leftarrow \text{UpdateReadoutWeights}(W^{out}, s^*, y^\mu, \eta, \kappa)$; // Readout update (Eqs. 83--84)
end

Inference: given new input x , compute $\hat{s} \leftarrow \text{EvolveUntilConvergence}(0, J, x, 0, \lambda_{\rightarrow})$; output $\hat{y} = W^{out} \hat{s}$ as prediction.;

Networks with arbitrary topology First, we generalize the learning algorithm, which was described for the core module in the main text, to recurrent networks with an arbitrary internal topology.

Assume that we are provided with a set of P patterns with their associated labels $\{x^\mu, y^\mu\}_{\mu=1}^P$ with $x^\mu \in \mathbb{R}^D, y^\mu \in \mathbb{R}^C$. Consider a generic recurrent network of binary neurons $s_1, \dots, s_N \in \{-1, 1\}$ that interact through a coupling matrix $J \in \mathbb{R}^{N \times N}$. Assume that the topology of the network is encoded via an adjacency matrix $A \in \{0, 1\}^{N \times N}$, such that $A_{ij} = 0$ implies $J_{ij} = 0$. Note that the core module and the multilayer chain model, among many others, can be represented this way by an appropriate choice of A and J .

As for the core module, we introduce projection matrices $W^{in} \in \mathbb{R}^{N \times D}$, $W^{back} \in \mathbb{R}^{N \times C}$ and $W^{out} \in \mathbb{R}^{C \times N}$. In general, not all neurons must be affected by the input or supervisory signal, nor affect the predicted output. We encode this with binary vectors $a^{in}, a^{back}, a^{out} \in \{0, 1\}^N$.

In this more general case, the network evolves in time according to the update rule:

$$s_i \leftarrow \text{sgn} \left(\sum_{j=1}^N A_{ij} J_{ij} s_j + a_i^{in} \lambda_x \sum_{k=1}^D W_k^{in} x_k^\mu + a_i^{back} \lambda_y \sum_{c=1}^C W_c^{back} y_c^\mu \right), \quad (79)$$

Like for the core module, when an equilibrium is reached, the supervisory signal is removed (set $\lambda_y = 0$), and the dynamics continues until a new fixed point is reached. Denote by s' and s^* the two internal states reached at the end of the two phases. The plasticity rule in the general case can be written as:

$$h_i = \sum_{j=1}^N A_{ij} J_{ij} s_j^* + a_i^{in} \lambda_x \sum_{k=1}^D W_k^{in} x_k^\mu \quad (80)$$

$$J_{ij} \leftarrow J_{ij} + A_{ij} \eta s_i^* s_j^* \mathbb{1}(s_i^* \cdot h_i \leq k) \quad (81)$$

The projection W^{in} can be learned using the same rule, modifying Eq. (81) appropriately: x_k^μ plays the role of s_j^* and a_i^{in} plays that of A_{ij} to update each component W_{ik}^{in} . In formulas:

$$W_{ik}^{in} \leftarrow W_{ik}^{in} + a_i^{in} \eta s_i^* x_k^\mu \mathbb{1}(s_i^* \cdot h_i \leq k) \quad (82)$$

As for the readout matrix, many options are possible, depending on the specific task at hand. In the case of classification, assuming y^μ is one-hot encoded using ones to signal the correct class and minus ones to signal the wrong ones, we can employ an analogous perceptron learning rule:

$$l_c = \sum_{j=1}^N a_j^{out} W_{cj}^{out} s_j^* \quad (83)$$

$$W_{cj}^{out} \leftarrow W_{cj}^{out} + a_j^{out} \eta y_c^\mu s_j^* \mathbb{1}(y_c^\mu \cdot l_c \leq k) \quad (84)$$

Note that learning the readout is completely decoupled from the synaptic plasticity affecting J and W^{in} . W^{out} could be left untrained until the very end of training, and then be learned offline, with completely equivalent results. Also

note that, to accurately reduce this general case to the core module or the multilayer chain model, we need to avoid updating J_D and/or λ .

In this general formulation, we can use A to encode the internal topology of the network. For example, we can generalize the multilayer chain model to allow nonzero couplings between any pair of neurons in subsequent layers (a ‘fully-connected’ multi-layer design). This corresponds to a ‘block-tridiagonal’ structure for A : each ‘block’ encodes the interactions (or lack thereof) between a pair of layers; A has ones exactly in all entries of all blocks lying along the main diagonal, the first subdiagonal and the first supradiagonal. We can also use the binary vectors $a^{in}, a^{back}, a^{out}$ to control the connectivity between the layers and the input/output. For example, we can introduce skip connections between intermediate layers and the input/output, or between distant layers.

We have experimented with these and other modifications to the network topology. Our preliminary results suggest that, provided the RM is present, the system exhibits nontrivial learning capabilities using the algorithm described. This flexibility is promising, since it means that it could be possible to introduce an inductive bias via the network topology (e.g., exploiting the spatial structure of images via convolutions).

Mini-batch training It is possible to group the data patterns into mini-batches of size B to speed up the training process, instead of showing the training examples one by one. The network relaxation is carried out independently for each pair (x^μ, y^μ) in the batch, in parallel, exploiting batched tensor operations. This provides fixed points $(s')^\mu$ and $(s^*)^\mu$ for each. Then, the couplings updates are computed independently and in parallel for each, and the individual updates are averaged along the batch dimension. In formulas, (80) and (81) become:

$$h_i^\mu = \sum_{j=1}^N A_{ij} J_{ij} (s^*)^\mu_j + a_i^{in} \lambda_x \sum_{k=1}^D W_k^{in} x_k^\mu, \quad \mu = 1, \dots, B \quad (85)$$

$$J_{ij} \leftarrow J_{ij} + \frac{\eta}{B} \sum_{\mu=1}^B A_{ij} (s^*)^\mu_i (s^*)^\mu_j \mathbb{1}((s^*)^\mu_i \cdot h_i^\mu \leq k) \quad (86)$$

Multilayer chain model We report here an observation about the synchronous update dynamics with the multilayer chain model. The synchronous dynamics allows to exploit the parallelism of modern computing hardware like GPUs. However, especially in the multilayer chain model, this fully parallel update can lead to the onset of cycles. Intuitively, this is because the strong positive couplings between pairs of neurons belonging to subsequent layers tend to keep swapping their states, if they initially differ. To mitigate this effect, when using the multilayer chain model, we introduce a hyperparameter $p \in (0, 1]$: at each time step, instead of updating all neurons at once according to (2), we update each neuron with probability p .

This simple strategy, which preserves the distributed character of the dynamics and does not require global coordination, is effective at avoiding limit cycles.

Approximate training scheme A key feature of the proposed training protocol is that, once the initial *supervised* fixed point s' is reached and the teaching signal is removed, the network state remains effectively stable—only the local pre-activation fields are altered. More formally, in Table III, we observe that:

$$\frac{1}{NP} \sum_{\mu=1}^P \sum_{i=1}^N s_i'^\mu s_i^{*\mu} \approx 1, \quad (87)$$

indicating that s' and s^* are nearly identical across patterns. Motivated by this observation, we propose an *approximated* training scheme where the unsupervised relaxation phase is removed entirely (Lines 5-6 in Algorithm 1). The local plasticity rule is then applied to stabilize the state s' , instead of s^* . Empirically, we find that this approximation preserves overall classification performance in networks with narrower hidden layers ($N \sim 400$), while wider networks ($N \sim 3200$) exhibit a measurable reduction in training and validation accuracies in the classification-optimal J_D regime; see Figure 6.

Notably, the approximate training scheme enables the network to learn input-output relations even at low self-coupling intensities ($J_D \sim 0.1$), which typically lead to unstable or chaotic dynamics in the full model. One contributing factor may be the absence of the separate unsupervised relaxation phase: in the approximate scheme, the system evolves under the simultaneous influence of both input and target fields (modulated by λ_x and λ_y , respectively), in addition to the self-interaction term J_D . This combined structure imposes stronger constraints on the dynamics and may help suppress chaotic behavior when J_D is weak.

Importantly however, this approximate variant of the learning algorithm is less realistic from a biological perspective. In fact, contrary to the algorithm presented in the main text, this variant effectively requires ignoring the contribution of the term $\lambda_y W^{back} y^\mu$ to the local field at the moment of the plasticity step. On the contrary, this ‘special treatment’

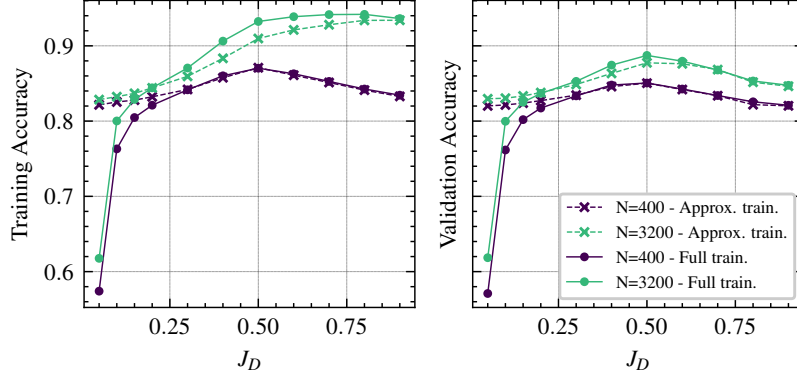


FIG. 6: Comparison of full and approximate training dynamics on the Entangled-MNIST dataset with $N = 400$ and $N = 1600$ for $J_D \in [0.1, 0.9]$. Results are averaged over two independent runs, each trained for 100 epochs. The approximate scheme omits the unsupervised relaxation phase by setting $s^* := s'$.

of the synapses providing output supervision at the time of plasticity is not necessary in the variant of the main text, which does not make any distinction in its treatment of the various synapses.

Local regularization Modern neural networks are typically trained by minimizing a task-specific loss function, which quantifies the discrepancy between predicted outputs and target labels. Beyond guiding learning, the choice of loss function implicitly shapes the geometry and robustness of the learned representations. For instance, the commonly used cross-entropy loss not only promotes correct classification but also encourages large decision margins between classes. This margin-based behavior has been linked to improved generalization and robustness, particularly in the presence of noise or adversarial perturbations. Other losses, such as hinge or contrastive losses, can be explicitly designed to enforce margin maximization or structural constraints on the embedding space. The proposed training protocol is not based on a global loss function, but can nonetheless accommodate for such kind of regularization by exploiting the local nature of its update rule. Specifically, we can introduce a surrogate to cross entropy loss in the couplings update rule (Eq. 9):

$$J_{ij} \leftarrow J_{ij} + \eta s_i^* s_j^* \left[-\frac{1}{2} + \frac{1}{2} \tanh(\gamma(s_i^* h_i - \kappa)) \right]. \quad (88)$$

Instead of simply increasing the stability margin conditionally on a threshold κ , we modulate synaptic updates based on a smooth function of κ that encourages both *correct* and *confident* predictions. In this way, the model inherits the generalization benefits of margin-based objectives, akin to those induced by cross-entropy, while remaining fully local and compatible with biologically plausible learning mechanisms.

Benchmark experiments details

In this section, we list the hyperparameters used for the benchmarking experiments reported in the main text. Optimal values were determined via a grid search, maximizing validation accuracy on a randomly selected holdout set of size $P = 6000$.

The grid search was conducted for a model width $N = 1600$, and optimality was tested at other widths by applying small perturbations. We found that the same hyperparameters remained optimal for $N = 100, 200, 400, 800, 3200$, but required retuning for $N = 6400$.

A notable observation concerns the role of λ_x . Comparable performance was achievable across a broad range $\lambda_x \in [2.0, 6.0]$ when J_D and λ_y were adjusted accordingly. We selected $\lambda_x = 5$ for the reported results, as it provided higher robustness to variations in the other two hyperparameters.

For the Random Features and Reservoir models, all hyperparameters remained optimal across all tested widths. We test these two models as special case of our full models. Specifically, the reservoir model is taken from the full model by setting $\eta_{W_{in}} = \eta_J = \lambda_y = 0$. The random features model is obtained by taking the reservoir model and setting the maximum amount of dynamics iterations $\max_{\text{iter}} = 1$.

The final chosen parameters are summarized in Table I.

Hyperparameter	$N = \{100, \dots, 3200\}$	$N = 6400$	Random Features	Reservoir
J_D	0.5	0.5	/	0.5
η_J	0.005	0.01	0.0	0.0
$\eta_{W_{in}}$	0.03	0.01	0.0	0.0
$\eta_{W_{out}}$	0.03	0.01	0.03	0.03
κ_J	1.4	1.8	/	/
$\kappa_{W_{in}}$	3.0	3.0	3.0	3.0
$\kappa_{W_{out}}$	3.0	3.0	3.0	3.0
λ_x	5.0	5.0	5.0	5.0
λ_y	0.9	0.7	0	0
n_{epochs}	200	400	200	200
\max_{iter}	5	5	1	5

TABLE I: Optimal hyperparameters for models used in benchmarking. Both random features and reservoir models can be seen as a special case of the full model with some specific components removed.

Importance of the stable regions

In this section, we report on the second set of experiments concerning the role of the RM geometry and accessibility. We consider the classification task on Entangled MNIST, and we consider several variants of our proposed algorithm. All variants are based on the core model and the learning algorithm discussed in the main text. First, we consider two variants that differ in the initialization of the internal couplings:

- **asym**: this is exactly the core model, with the internal coupling matrix initialized sampling each off-diagonal component i.i.d. from a Gaussian, $J_{ij} \sim \mathcal{N}\left(0, \frac{1}{\sqrt{N}}\right)$, and diagonal entries equal to J_D .
- **sym0**: the coupling matrix is initialized symmetrically: sample J like for the **asym** baseline, and then use $(J + J^T)/2$.

Additionally, we consider two more variants that use the same initialization as in **sym0**, but additionally implement a variant of the update rule (9) that preserves the initial symmetry:

- **sym1**: Condition the update of J_{ij} on both s_i and s_j not being stable enough, instead of s_i only. Training with batches of examples, this is done independently for each example in the batch. In formulas:

$$J_{ij} \leftarrow J_{ij} + \eta s_i^* s_j^* \mathbb{1}(s_i^* \cdot h_i \leq k \ \& \ s_j^* \cdot h_j \leq k)$$

Note that we have omitted A_{ij} since the core model is fully connected.

- **sym2**: Update J_{ij} using the average of the updates that (9) would have made for J_{ij} and J_{ji} . In formulas:

$$J_{ij} \leftarrow J_{ij} + \frac{1}{2} \eta s_i^* s_j^* \mathbb{1}(s_i^* \cdot h_i \leq k) + \frac{1}{2} \eta s_i^* s_j^* \mathbb{1}(s_j^* \cdot h_j \leq k)$$

We consider $J_D = 0.0, 0.5$ and we compare the average performance on Entangled MNIST of the methods across 3 seeds. The results are shown in Figure 7. The key observation is that, while symmetry has little-to-no impact on performance, despite the dynamics being convergent from the beginning of training, introducing a self-coupling leading to the onset of the accessible clusters of fixed points described, produces a drastic improvement in performance for the asymmetric baseline and the symmetric variants alike.

Evolution of symmetry

In this section, we describe how the degree of symmetry of the internal-couplings matrix evolves as training progresses, with symmetric or asymmetric initialization. The models considered thus correspond to those called **asym** and **sym0** in the previous section.

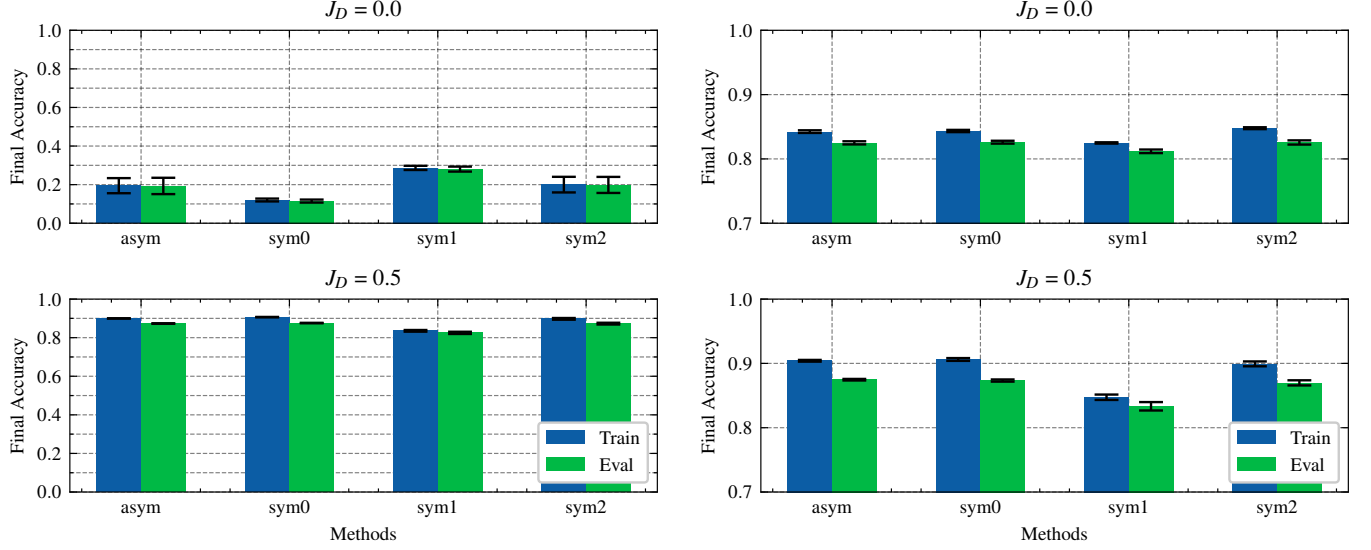


FIG. 7: Impact of the existence of the accessible stable region vs symmetry of the internal couplings on performance on Entangled MNIST for the core model. **Left:** Algorithm described in the main text (two-phase dynamics). **Right:** Algorithm variant described in this section (ignoring right fields for update).

To quantify the symmetry level of a square matrix of internal couplings J , we use the following metric. We decompose J into its symmetric and anti-symmetric part, according to

$$J = S + A = (J + J^T)/2 + (J - J^T)/2$$

It can be shown that S so defined is the best symmetric approximation of J in the Frobenius sense. Then, we use

$$\rho = (||S|| - ||A||)/(||S|| + ||A||)$$

as a measure of the symmetry level of J . ρ is normalized between -1 and 1 ; it equals 1 when the matrix is perfectly symmetric and -1 when it is perfectly anti-symmetric. A matrix with random iid entries from a Gaussian has a score close to 0 . We show the evolution of the symmetry level during training in Figure 8.

Landscape analysis

The local entropy analysis predicts that the models exhibit a RM for J_D or λ large enough. We study how the training process affects this landscape by analyzing a finite-size network ($N = 1600$, $L = 1$) trained on the Entangled-MNIST dataset with the hyperparameters reported in Table II.

Hyperparameter	N	L	J_D	η_J	$\eta_{W_{in}}$	$\eta_{W_{out}}$	κ_J	$\kappa_{W_{in}}$	$\kappa_{W_{out}}$	λ_x	λ_y	n_{epochs}
Value	1600	1	0.5	0.005	0.01	0.01	$0.9 + J_D$	3.0	3.0	2.0	0.9	30

TABLE II: Hyperparameters for the Entangled-MNIST landscape analysis. The trained network achieved 88.54% training accuracy and 85.92% validation accuracy.

We select a random subset of $P = 2000$ training inputs $\{x^\mu\}_{\mu=1}^P$. For each x^μ , we compute the corresponding stable state $\hat{s}^{*\mu}$ by iterating the dynamics update rule

$$s_i \leftarrow \text{sign} \left(\sum_{j \neq i} J_{ij} s_j + J_D s_i + \lambda_x x_i^\mu \right) \quad (89)$$

until convergence.

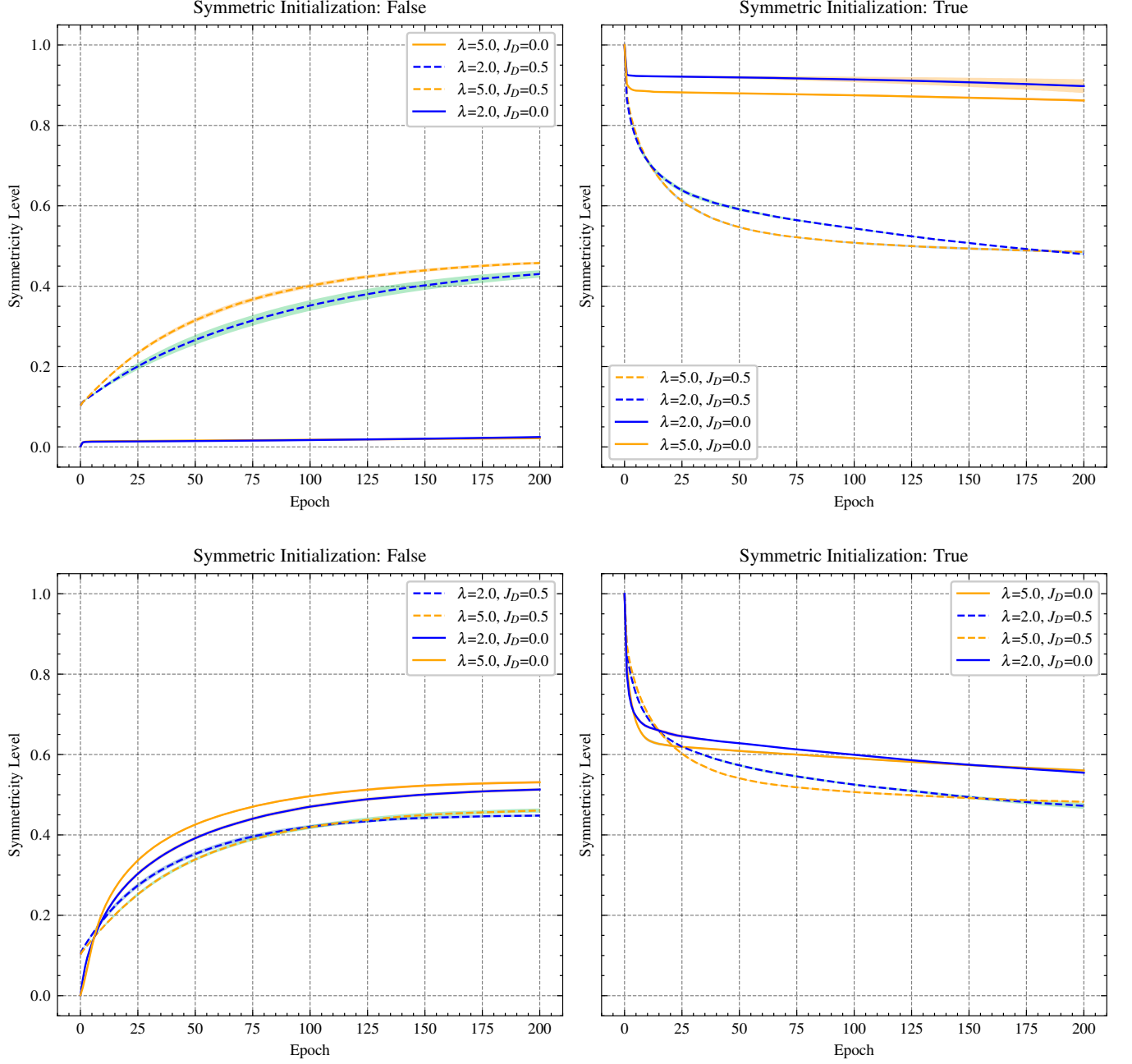


FIG. 8: Evolution of the symmetry level of the matrix of internal couplings during training for the core model. Left shows asymmetric initialization, right shows symmetric initialization. **Top:** two-phase dynamics (main text). **Bottom:** variant ignoring right fields for update.

To assess connectivity between two stable states $(\hat{s}^{*\mu}, \hat{s}^{*\nu})$, we construct intermediate input configurations $x_\tau^{\mu\nu}$ with $\tau \in [0, 1]$ drawn uniformly from

$$\left\{ x \in \{-1, +1\}^N \mid \frac{d(x, x^\mu)}{d(x^\mu, x^\nu)} = \tau \right\}, \quad (90)$$

where $d(\cdot, \cdot)$ is the Hamming distance. Evolving $x_\tau^{\mu\nu}$ under (89) gives the intermediate fixed point $\hat{s}_\tau^{\mu\nu}$.

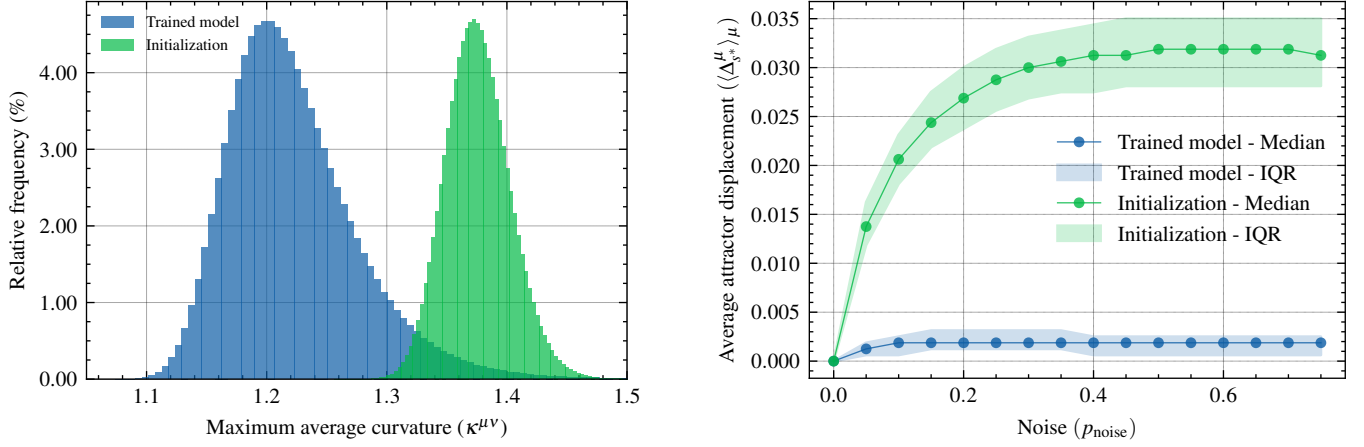


FIG. 9: (a) Distribution of the maximum normalized geodesic curvature $\kappa^{\mu\nu}$ between stable attractors, before (green) and after (blue) training. Training reduces typical curvature, indicating straighter connecting paths. (b) Distribution of the attractor displacement $\Delta_{s^*}^{\mu}$ as a function of the noise injected into $\hat{s}^{*\mu}$, showing increased robustness post-training. The median is plotted together with the 25th-75th percentile range (IQR).

We quantify deviations from a geodesic path in state space through the *normalized path curvature*

$$C^{\mu\nu}(\tau) = \frac{d(\hat{s}^{*\mu}, \hat{s}_{\tau}^{*\mu\nu}) + d(\hat{s}_{\tau}^{*\mu\nu}, \hat{s}^{*\nu})}{d(\hat{s}^{*\mu}, \hat{s}^{*\nu})}. \quad (91)$$

For each pair, we take the maximum along the path,

$$\kappa^{\mu\nu} = \max_{\tau \in (0,1)} \mathbb{E}[C^{\mu\nu}(\tau)], \quad (92)$$

where $\mathbb{E}[\cdot]$ is the empirical average over resamplings of $x_{\tau}^{\mu\nu}$.

Figure 9(a) shows a significant distribution shift of $\kappa^{\mu\nu}$ after training: from mean 1.367 (s.d. 0.027) at initialization to mean 1.222 (s.d. 0.055) post-training. Values close to one imply that intermediate attractors lie near the shortest Hamming path between endpoints, suggesting that training tends to create low-curvature corridors connecting attractors associated with different inputs.

To characterize these connections more directly, we compute the *normalized trajectory distance*

$$D^{\mu\nu}(\tau_1, \tau_2) = \frac{d(\hat{s}_{\tau_1}^{*\mu\nu}, \hat{s}_{\tau_2}^{*\mu\nu})}{d(\hat{s}^{*\mu}, \hat{s}^{*\nu})}. \quad (93)$$

Representative cases in Fig. 10 show that, after training, the trajectories between attractors exhibit reduced length and curvature, in agreement with the global curvature statistics reported in Figure 9(a).

We also assess local robustness by perturbing each stable state with spin-flip noise:

$$s_{\text{noise}}^{\mu} = \hat{s}^{*\mu} \odot \xi_{p_{\text{noise}}}, \quad \xi_i \sim \text{Rademacher}(p_{\text{noise}}),$$

where p_{noise} is the flip probability. From s_{noise}^{μ} , we evolve the system with the update rule in Equation 89 to its fixed point $\tilde{s}^{*\mu}$ and measure the *attractor displacement*

$$\Delta_{s^*}^{\mu} = d(\hat{s}^{*\mu}, \tilde{s}^{*\mu}).$$

The distribution of $\Delta_{\text{att}}^{\mu}$ [Fig. 9(b)] shifts toward smaller values after training, indicating greater stability to perturbations. Even before training, displacements remain fairly small ($< 5\%$), consistently with the presence of highly entropic clusters of stable attractors, whose basin of attraction is determined by the left field.

Taken together, the evidence suggests that training reorganizes the RM by shortening and straightening inter-attractor paths, enlarging the effective reach of individual attractors, and improving robustness to perturbations.

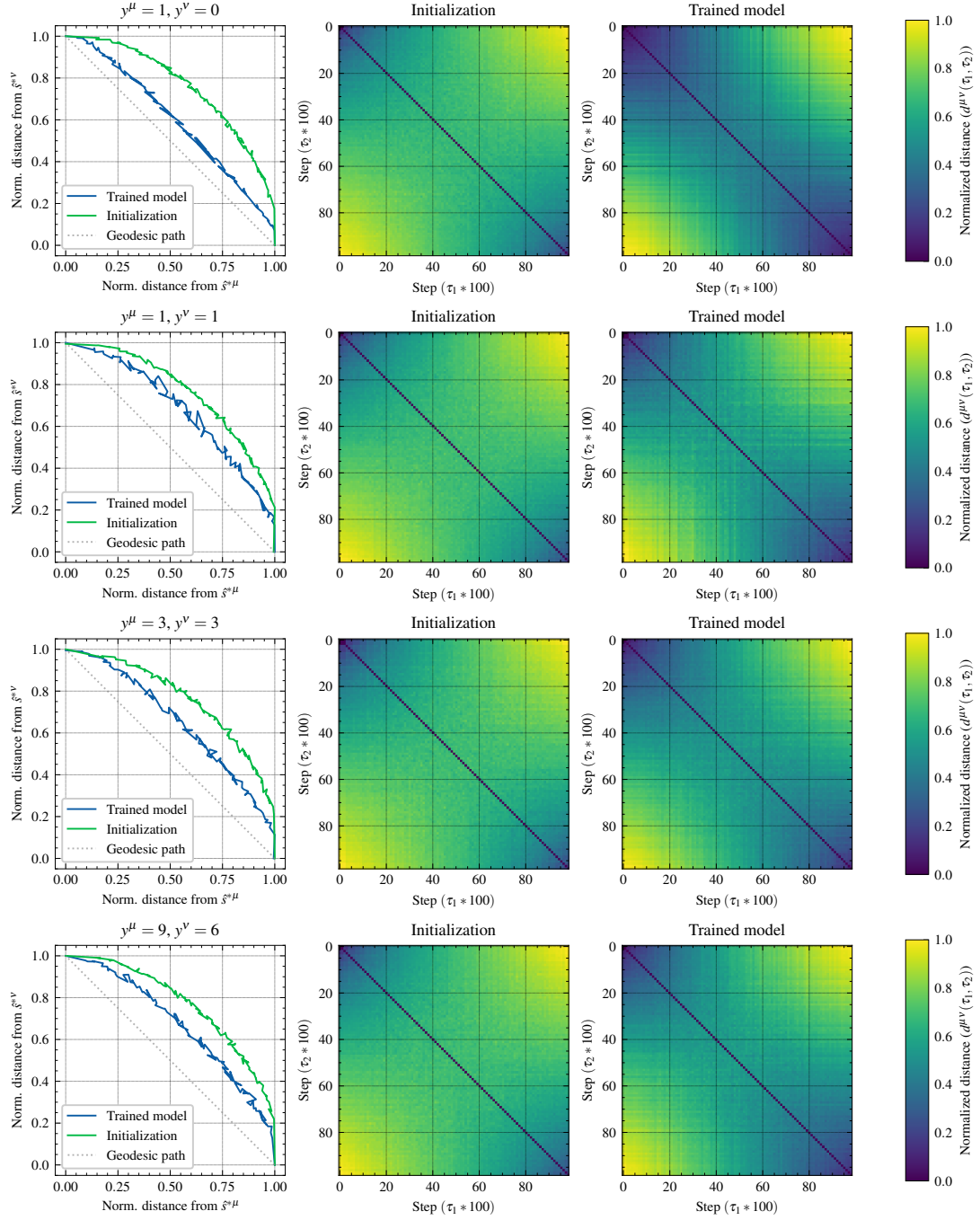


FIG. 10: Pairwise normalized distances $d^{\mu\nu}(\tau_1, \tau_2)$ along interpolated trajectories between two training examples $(x^\mu, y^\mu), (x^\nu, y^\nu)$. After training, trajectories show shorter paths, closer to the actual geodesic.

Evolution of internal states

The learning process consists in an iterated stabilization of the network attractors, carried via the perceptron rule. The network dynamics undergoes a first supervised phase, where a stable state s' is reached, followed by an unsupervised phase ($\lambda_y=0$), where the network reaches the final attractor s^* . The success of this learning process is implicitly based on the observation that, when switching between supervised and unsupervised relaxation, the stable configurations remain almost unaltered. Only the local fields change. In other words, in order to have an effective supervising signal, s' and s^* must be highly correlated.

To verify directly this scenario, we analyze the internal states of the network at different stages of training. Specifically, we study the *overlap* between the network states s' and s^* , which correspond to the fixed points reached during the supervised and unsupervised phases, respectively (see Algorithm 1).

The average overlap on the dataset is defined as:

$$q_{\text{dyn}} = \frac{1}{NP} \sum_{\mu=1}^p \sum_{i=1}^N s_i'^{\mu} s_i^{*\mu},$$

We evaluate the distribution of overlaps during learning using a single-layer network ($L = 1$) with $N = 1600$ neurons, trained on the Entangled-MNIST dataset. We vary the strength of internal coupling (J_D), input field (λ_x), and right field (λ_y). For each setting, we measure the overlap distribution at initialization, after the first epoch, and at the end of training (epoch 20).

Results are summarized in Table III.

J_D	λ_x	λ_y	Initialization	Epoch 1	Epoch 20
0.5	5.0	0.9	0.930 [0.921, 0.938]	0.991 [0.987, 0.995]	0.996 [0.993, 0.999]
0.5	5.0	0.5	0.975 [0.970, 0.980]	0.998 [0.996, 0.999]	0.999 [0.999, 1.000]
0.5	2.0	0.9	0.761 [0.744, 0.779]	0.995 [0.991, 0.998]	0.999 [0.996, 1.000]
0.5	2.0	0.5	0.892 [0.877, 0.907]	0.999 [0.998, 1.000]	1.000 [0.999, 1.000]
0.0	5.0	0.9	0.862 [0.852, 0.871]	1.000 [0.999, 1.000]	1.000 [1.000, 1.000]
0.0	5.0	0.5	0.915 [0.907, 0.922]	1.000 [1.000, 1.000]	1.000 [1.000, 1.000]
0.0	2.0	0.9	0.649 [0.634, 0.664]	1.000 [1.000, 1.000]	1.000 [1.000, 1.000]
0.0	2.0	0.5	0.748 [0.734, 0.761]	1.000 [1.000, 1.000]	1.000 [1.000, 1.000]

TABLE III: Average overlap q_{dyn} between the network states s' (supervised phase) and s^* (unsupervised phase) across training. Each entry reports the median overlap and its 5th-95th percentile range over the training set of Entangled-MNIST. We vary the self-coupling strength J_D , left field λ_x , and right field λ_y , and track the evolution of the overlap at initialization, after the first training epoch, and after 20 epochs.

Optimal training performance (training accuracy 91%, validation accuracy 87%) is obtained with $J_D = 0.5$, $\lambda_x = 5.0$ and $\lambda_y = 0.9$ (first row). Any model with $J_D = 0.0$ is unable to learn effectively (training/validation accuracy ~ 0.1). The results show that the learning scheme improves the stability of fixed points already after the first epoch. Moreover, optimal learning occurs when the supervisory signal is strong enough to nudge the attractor without fully overriding the intrinsic dynamics. Lastly, the results suggest that stabilizing attractor states alone is not sufficient for successful learning, emphasizing the importance of attractor geometry for the classification task.

In addition to the evolution of the network configuration during the relaxation dynamics, it is natural to wonder about the evolution of the internal representations associated with each input-output pair throughout training. To explore this aspect, we consider a random subset of $P = 300$ patterns from Entangled-MNIST and we measure the similarity (1 minus the Hamming distance) between the internal representations associated to different patterns before and after training. To visualize the data, we order the patterns by label (first all zeros, then all ones, etc.) and we use a heatmap to encode the similarity matrix.

More precisely, let x_μ and x_ν be two patterns with indexes μ and ν in the chosen ordering. We run inference with the model on x_μ , which consists in letting the network relax under the influence of x_μ as left external field, and without any right external field, until convergence. We obtain an internal representation s_μ^* for x_μ ; we do the same for x_ν to obtain s_ν^* . The entry (μ, ν) of the similarity matrix is: $S_{\mu\nu} = 1 - d(s_\mu^*, s_\nu^*)$. We compute the similarity matrix before and after training; for visualization purposes, we shift all values of all similarity matrices by a single mean value, computed averaging across pattern pairs and across time. The results are shown in Figure 11. Two trends are observed, comparing representations before and after training: first, the representations of different patterns tend in general to get closer together, occupying a cone in state space; and second, the representations become strongly clustered based on label (evidenced by the checker structure of the matrix) with patterns sharing the same label being significantly more similar to each other than patterns having different labels.

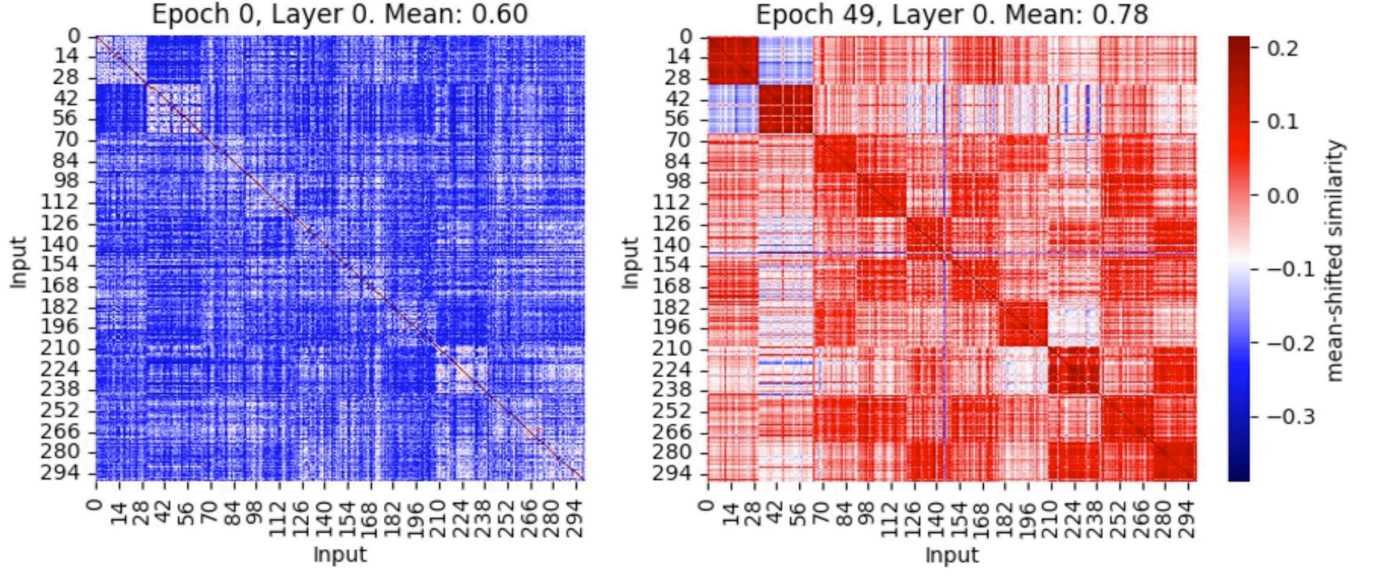


FIG. 11: Similarity matrix of the internal representations of a fixed set of 300 patterns from Entangled MNIST before (**left**) and after (**right**) training. Patterns are ordered according to their label. The similarity measure used is one minus the hamming distance; the similarities are shifted by a single mean value, in such a way that colors remain consistent across time. The mean value reported on top of each heatmap is the average similarity across all pairs at that time, not shifted.

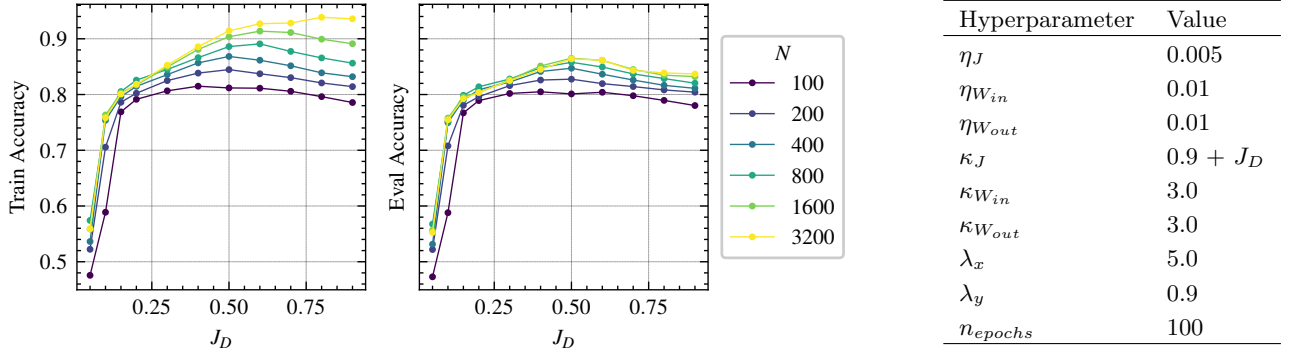


FIG. 12: (a) Training and evaluation accuracy as a function of the self-coupling parameter J_D for various hidden layer sizes $N \in \{100, 200, 400, 800, 1600, 3200\}$. The network shows optimal performance for intermediate values of J_D , with larger models benefiting more from self-coupling. (b) Hyperparameter configuration used across all experiments.

Impact of J_D on training performance

In this section, we discuss the important effect of the self-coupling constant J_D on training performance. To do so, we train our recurrent neural network on the Entangled-MNIST dataset while varying the value of J_D in the interval $[0.05, 0.9]$. In accordance with the main text, we choose $L = 1$ and $N \in \{100, 200, 400, 800, 1600, 3200\}$. We train all models using an identical set of hyperparameters, detailed in Figure 12. Training and validation accuracies are reported in Figure 12.

As expected, we observe optimal performance at intermediate values of J_D . In the limit $J_D \rightarrow 0$, the RM geometry collapses, and the model effectively regresses to random guessing. On the other hand, as $J_D \rightarrow \infty$, the internal dynamics lose their discriminative capacity, since every state becomes a stable fixed point. In this regime, the network effectively behaves as a random feature model, as the internal state s at time $t = 1$ becomes fully determined by the input ξ^μ (or more generally, by its projection $W_{in}\xi^\mu$).

Between these two extremes, however, lies a nontrivial intermediate regime where the RM remains exploitable and

the internal dynamics play a meaningful role in shaping the model’s performance. Additionally, we find that increasing the hidden layer size N enhances trainability and stabilizes training accuracy across a broader range of J_D , although the accuracy gains are more pronounced with training patterns than it is for unseen ones.

Finally, we note that the optimal value of J_D depends on multiple factors, the most prominent being the input coupling strength λ_x .